Analysis of LHC Beam Gas Ionization monitor data and simulation of the electron transport in the detector

MARCIN PATECKI

Master Thesis

Supervisor:
dr Mariusz Sapiński
CERN - European Organization for Nuclear Research

Supervisor at Faculty of Physics, Warsaw University of Technology:
prof. nzw. dr hab. inż. Adam Kisiel

Warsaw, September 2013

Abstract

Since July 2012 I had an honor to work in the European Organization for Nuclear Research (CERN) as a member of the Technical Student Programme. This thesis presents the research concerning the electron transport in the Beam Gas Ionization (BGI) monitor in order to study the effects of the electrons interaction with a high energy particle beam.

In the first chapter the Beam Gas Ionization monitor is described together with its operating principle to give an overview of the analyzed detector. Chapter 2 contains the introduction to the transverse beam dynamics in the particle accelerator which is the theoretical background for the emittance measurements. The analyzed BGI data are presented in chapter 3. As the research was based on the computer simulations, its description together with the results are given in the chapter 4. Finally the chapter 5 contains the investigation of the magnetic field threshold in the BGI electron dynamics.

In very short words the Beam Gas Ionization monitors installed in the CERN LHC make use of the ionization of a small volume of the injected neon gas by the circulating beam. The electrons produced are guided towards the readout system using a combination of electric and magnetic fields. In the presence of the beam field their tracks are modified and the resulting profile is distorted. The Geant4 particle simulation package is used to simulate the ionization process, while the CERN developed PyECLOUD code is used for tracking of the resulting ionized particles.

It turned out that the space charge effects of the beam strongly affect the electron distribution of the liberated electrons. The profile broadening and distortion therefore occur which causes the wrong indications of the BGI monitors. Those effects strongly depend on the beam density which is defined by the bunch intensity and the beam size. It is important to mention that those phenomena occur only for proton beam which is more intense than the ion beam.

By running the simulations it was found that the stronger magnetic field dumps the space charge effects. The simulations have shown that a magnetic field of $1\ \mathrm{T}$ is enough to reproduce the beam profile correctly and obtain right value of the beam emittance. The further investigation of this issue resulted in obtaining the empirical formula for magnetic field threshold needed to keep the space charge effects at the expected level.

The performed research is a justification for possible BGI magnet exchange in order to ensure the correct operation also for a proton beam.

Contents

Chapter 1

Introduction

The European Organization for Nuclear Research, known as CERN [1], is an international organization focused on researching the fundamental physics. Established in 1954 and situated on the Franco-Swiss border, the organization has twenty European member states. With around 2400 full-time employees and 10000 visiting scientists representing over 600 universities and 113 nationalities, CERN is the largest particle physics laboratory in the world.

In this chapter the main CERN's tool, the Large Hadron Collider, will be introduced together with the four main experiments. The short description of the Beam Gas Ionization monitor, which is the main field of my interest, will be also presented.

1.1 The Large Hadron Collider

The Large Hadron Collider (LHC) is the world's largest and highest-energy particle accelerator build by CERN. It lies in a circular tunnel of 27 km in circumference, 50 to 175 meters beneath the Franco-Swiss border near Geneva, Switzerland. The LHC is a synchrotron which accelerates two beams of particles in opposite directions in separate beam pipes. It is designed to accelerate particles to collide with energies at the center of mass up to $\sqrt{s} = 14$ TeV for protons and $\sqrt{s} = 5.52$ ZTeV for lead ions.

The LHC is supplied with protons coming from the injector chain shown in the figure 1.1. The protons generated in the Duoplasmatron source are injected into the Linac2, which is a Alvarez-type linear accelerator, where protons are accelerated to 50 MeV and grouped in buckets by the radio frequency cavities. The next step is to inject the protons in the Proton Synchrotron Booster (PSB), a 157 m circumference device capable of accelerating high intensity beams up to 1.4 GeV. From the PSB the particles are transferred to the Proton Synchrotron (PS), a 628 m circumference ring, where they are accelerated to 26 GeV. Then particles go 50 m underground to the Super Proton Synchrotron (SPS), which has a circumference of 6.9 km and accelerates the protons to 450 GeV. The injector chain finishes with two transfer lines which

create the two beams circulating in LHC in opposite directions.

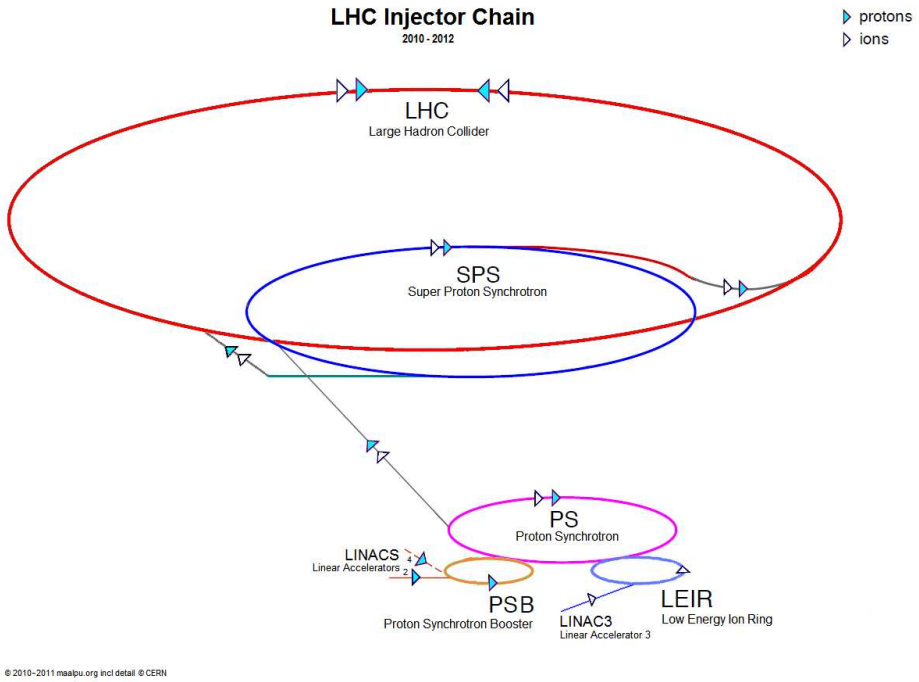

Figure 1.1: Schematics of the CERN injection chain.

1.2 The LHC Experiments

There are four main experiments at the LHC: ALICE, ATLAS, CMS, LHCb.

ALICE

ALICE (A Large Ion Collider Experiment) [2] is an experiment optimized to study heavy-ion collisions, especially the properties of strongly interacting matter, the phase transition to the Quark-Gluon Plasma and the phase diagram of hadronic matter.

ATLAS

ATLAS (A Toroidal LHC Apparatus) [3] is, together with CMS, one of two general purpose experiments at the LHC. The main goal of this experiment is to search for the Higgs bosons and the origin of mass. It also explores physics beyond the Standard Model e.g. extra dimensions of space, supersymmetry, evidence of the existence of dark matter and dark energy in the Universe.

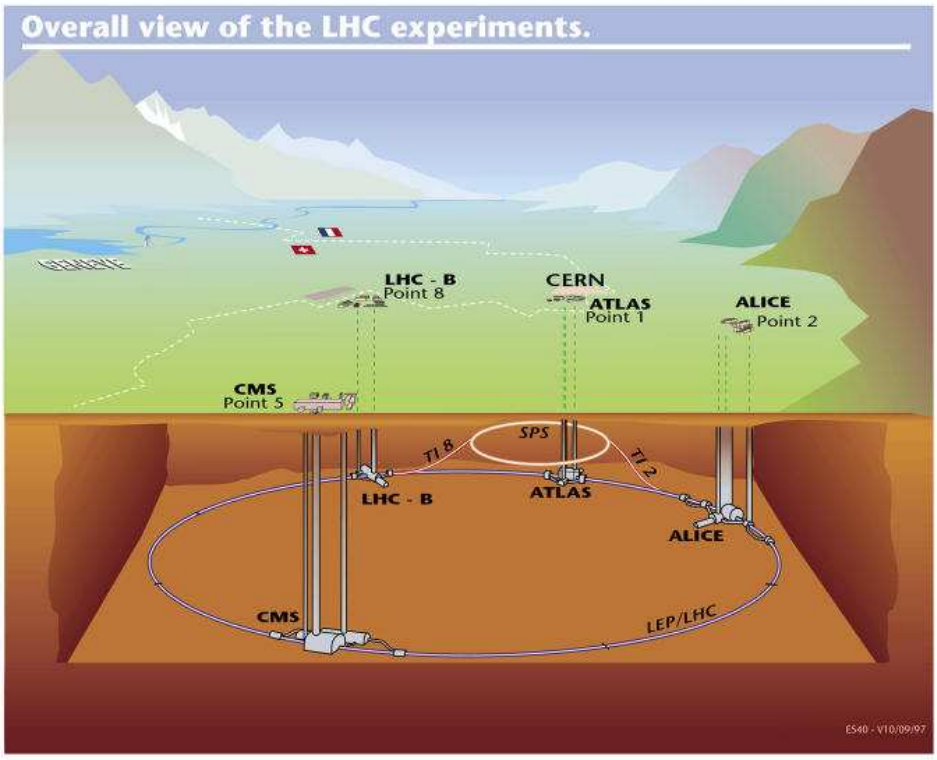

Figure 1.2: Artist's view of the CERN site on surface and underground, highlighting the LHC tunnel and the four particle detectors ALICE, ATLAS, CMS and LHCb.

CMS

CMS (Compact Muon Solenoid) [4], like ATLAS, is a general purpose experiment with similar to ATLAS goals. These two experiments complement each other but are designed and optimized in a different way to ensure cross-check of the measurements.

LHCb

LHCb (Large Hadron Collider beauty) [5] is a specialized experiment, particularly aimed at measuring the parameters of CP (charge conjugation and parity symmetry) violation in the interactions of hadrons composed of beauty hadrons. It investigates the slight difference between matter and antimatter by studying bottom quarks.

1.3 The Beam Gas Ionization Monitor

The Beam Gas Ionization monitors (BGI) [6] operating at the Large Hadron Collider at CERN is a beam instrument design for beam size measurements. The beam profiles are obtained by collecting the products of residual gas ionization occurring when the beam passes through the imperfect vacuum of the chamber. Figure 1.3 presents the picture of the BGI in the LHC.

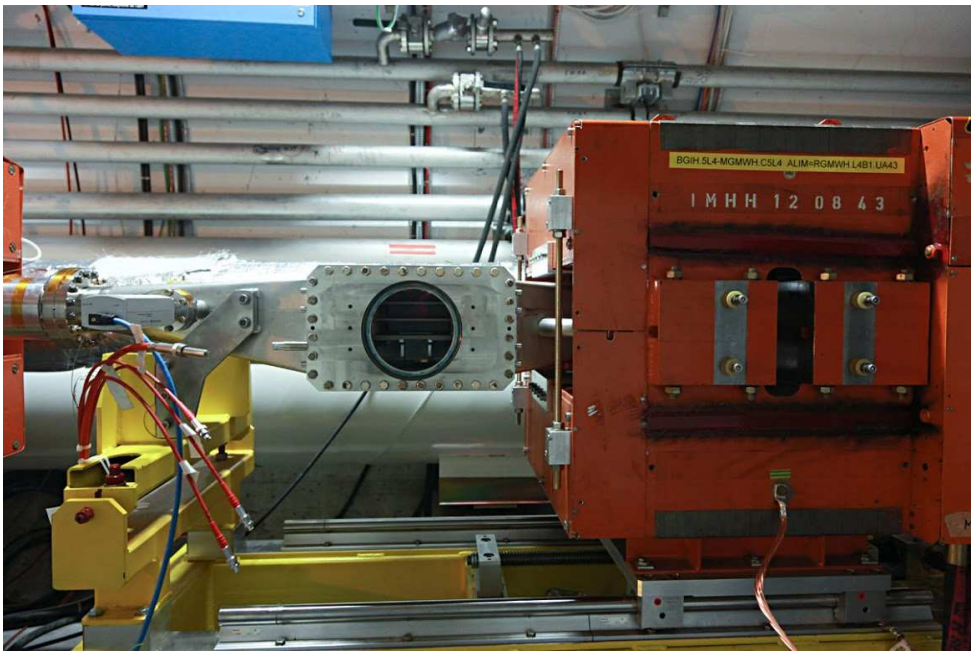

Figure 1.3: BGI in LHC. The magnet is shifted to show the chamber and optical port.

The BGI operating principle

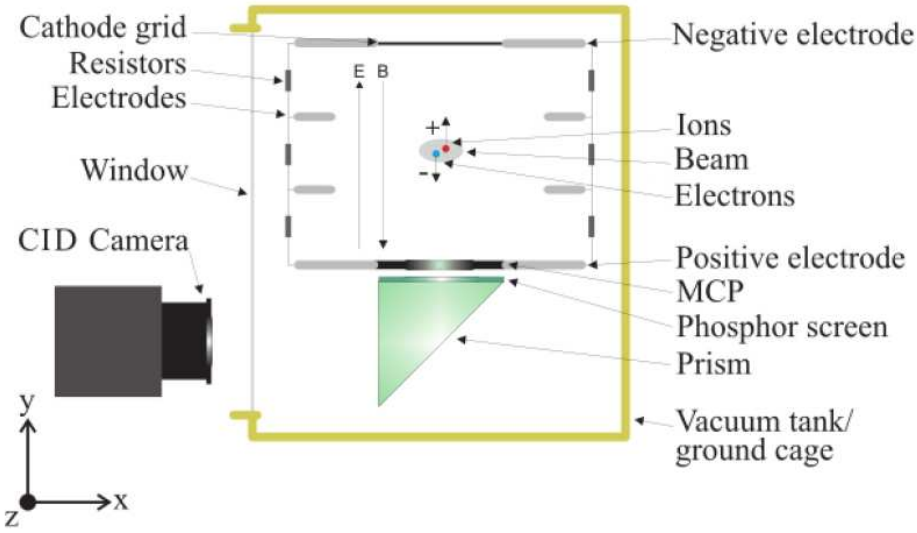

Figure 1.4: Sketch of the operating principle.

A cut through the BGI ionization chamber (figure 1.4) will be used for explaining the operating principle. We assume that the beam is passing in the z-direction, into the paper. As the chamber is filled with the low pressure (10^{-8} mbar) Neon gas, the circulating beam liberates the electrons and ions by the ionization process. They are then guided down and up respectively, due to the electric field generated by the two ceramic electrodes with a difference of potential of 4 kV. The distance between the cathode and anode is 85 mm. The lateral electrodes are

used to ensure the homogeneity of the electric field, which is necessary to preserve the spatial distribution of the electrons drifting through the chamber.

The orange magnet seen on the figure 1.3 is responsible for creating the constant magnetic field of 0.2 T in the y-direction. The electrons with the momentum obtained in the ionization process and due to interactions with a beam are therefore forced to follow the spiral trajectory. It should prevent the electrons from getting the transverse spread in space.

When the electrons reach the anode, they hit the Micro Chanel Plate (MCP) used for multiplying the number of electrons. The MCP is a 0.5 mm thin plate, usually made from the lead glass, where the electron multiplayers (called *channels*) are densely spaced and oriented parallel to each other (see figure 1.5). A high voltage is applied across the channels, so an incoming electron reaching a channel generate a cascade of electrons inside the channel. As the result, the electrons are multiplied with a gain of around $10^3 - 10^4$ which allows to obtain the clear signal.

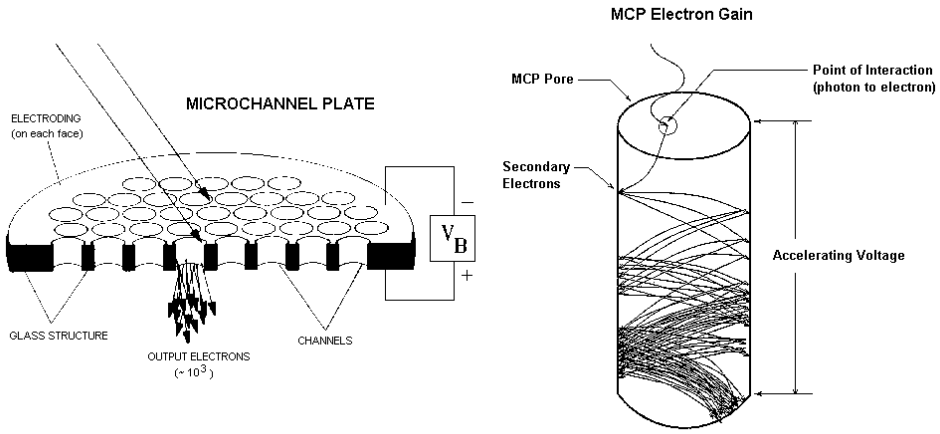

Figure 1.5: The operating principle of MCP [7].

The optical and control systems

Electrons leaving the MCP hit the phosphor screen located 2 mm behind the MCP. As the result, the electron distribution is converted into a photon distribution which is then transmitted via an optical system to a CID camera [8]. The optical system composed of several lenses and prisms is located outside the vacuum tank, making modifications to the imaging system simpler. The justification for using the optical system for electron detection is that it provides better resolution than for example mutli-strip anode, which was also considered during the design. The disadvantage of the optical system is that it produces an additional spread of the profile. Second drawback is the magnification of the optical system which is another limitation for the

detection resolution. The calibrated size of the pixel in the optical system is around $110\ \mu\mathrm{m}$. The example image of the beam taken by the BGI is shown on figure 1.6.

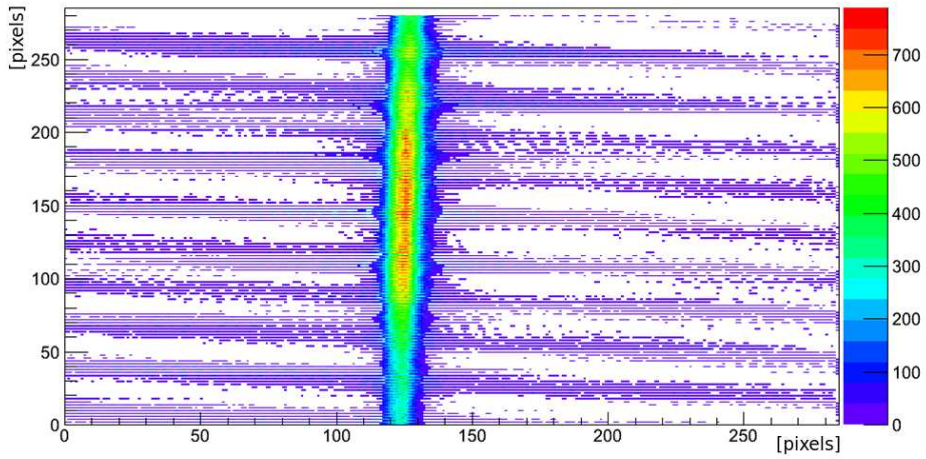

Figure 1.6: The example image of the beam taken by the vertical BGI monitor.

CID stands for Charge Injection Device which is an imaging array of photosensitive pixels, each of which contains a sense gate for integrating photogenerated charge during the course of a frame and an amplifier transistor for sampling voltage on the sense gate. Every pixel in a CID array can be individually addressed via electrical indexing of row and column electrodes. Unlike Charge Coupled Device (CCD) cameras which transfer collected charge out of the pixel during readout (and hence erase the image stored on the sensor), charge does not transfer from site to site in the CID array. Instead, a displacement current proportional to the stored signal charge is read when charge ”packets” are shifted between capacitors within individually selected pixels. Readout is non-destructive because the charge remains intact in the pixel after the signal level has been determined. To clear the array for new frame integration, the row and column electrodes in each pixel are momentarily switched to ground releasing, or ”injection” the charge into the substrate. The readout procedure is sketched on figure 1.7.

The main reason to use the Charge Injection Device (CID) instead of Charge Coupled Device (CCD) or Complementary Metal–Oxide–Semiconductor (CMOS) imaging array is that the first one can be configured as a radiation-hardened device that operates reliably in a wide range of radiation environments beyond the typical lifetime of CCD- or CMOS-based cameras – in some cases, by orders of magnitude. The basic idea behind radiation hardness is that charge-trapping centers in CID devices are neutralized by electrons from injected charge. Figure 1.8 shows the comparison of an image taken by CCD and CID cameras exposed to radiation of Co^{60} gamma source. It justifies a choice of CID cameras in the BGI monitors.

In order to improve the radiation hardness, the cameras used in LHC generate analog video signal which is less prone to electromagnetic interferences, can be transmitted over several-

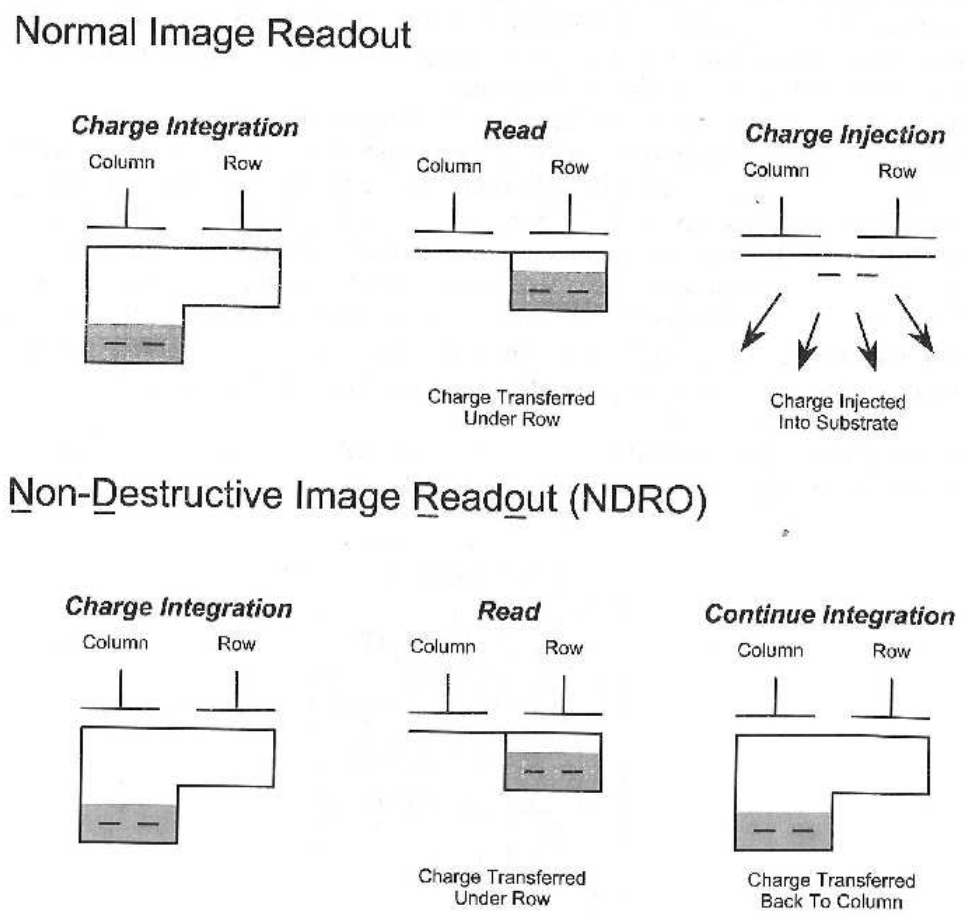

Figure 1.7: The normal (up) and non-destructive (bottom) readout procedure [8].

hundred meter cables and demand less radiation-sensitive electronic elements in the tunnel.

The BGI control system is divided into following subsystems:

1. the vacuum conditions and gas injection controlled by the central LHC vacuum system;
2. the high voltage is controlled by a cern-made VME card;
3. the camera settings are controlled via user application and send to the device by ETHERNET-to-RS485 converter (LANTRONIX UDS 1100);
4. the camera analog signal is captured, digitized and send to the user by cern-made VME card called BTV containing a frame grabber.

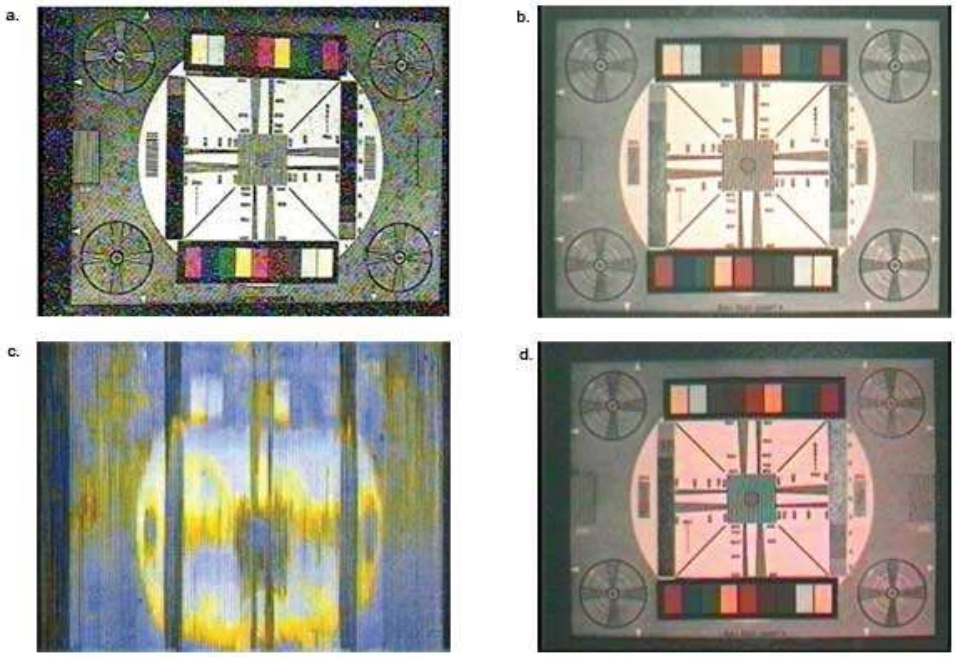

Figure 1.8: Images from a commercial CCD camera and the standard CID8825DX6 camera when exposed to a gamma source (Co^{60}): a and b show the CCD and CID images, respectively, with no radiation exposure. Image c shows deterioration in the CCD image after just 1 h of radiation exposure, but the CID image in d is much less affected after 45 h of exposure.[9].

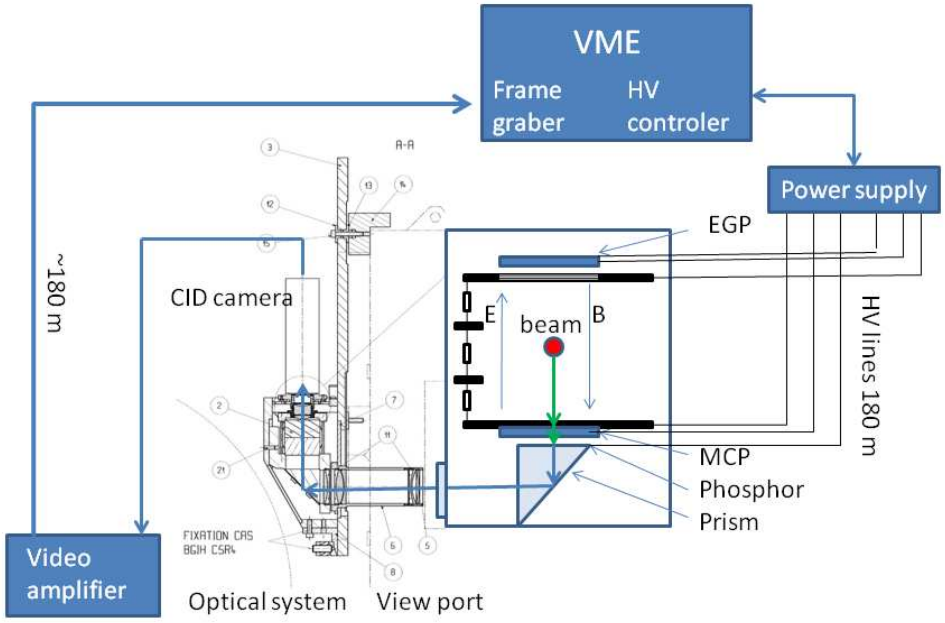

Figure 1.9: The sketch of BGI readout and high voltage control system [10].

Chapter 2

Theoretical overview

The Beam Gas Ionization monitors are design to measure the transverse beam emittance. In this chapter the theoretical overview of the transverse beam dynamics will be given [11], [12], [13]. The definition and properties of the transverse emittance will close this chapter.

2.1 The Coordinate System

Every accelerator has defined the ideal particle trajectory called the design orbit. It can be a straight line (linac), a spiral (cyclotrons), or a succession of arcs and straight lines (synchrotron). The particle following the design orbit is called the reference particle. For simplicity an ideal circular orbit of a radius ρ will be considered, see figure 2.1.

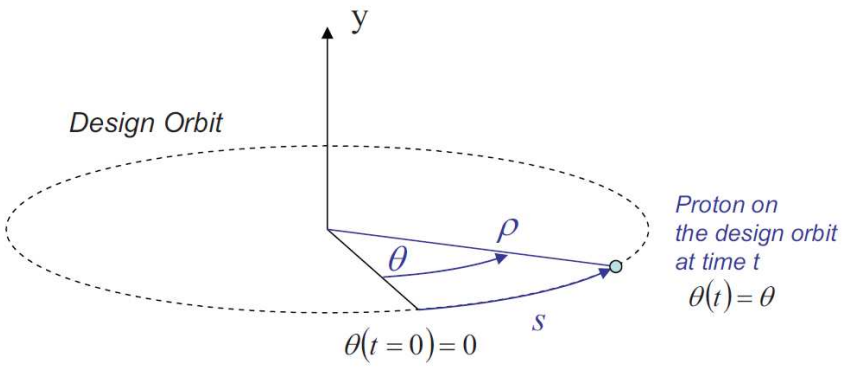

Figure 2.1: Sketch of a proton on the ideal design orbit of a circular accelerator [12].

The coordinates of any particle in the accelerator are defined in respect to the position of the reference proton at time t (see figure 2.2). It imposes the use of the cylindrical coordinate system $(r = \rho + x, \theta, y)$, based on the orthonormal frame $(\vec{u_x} = \vec{u_\rho}, \vec{u_s} = \vec{u_\theta}, \vec{u_y})$. The derivation of a given function f with respect to t will be noted $\dot{f}$ and the derivative of this function f with

respect to s will be noted f'. Since $s = vt$ we have

$$\dot{f} = \frac{df}{dt} = \frac{df}{ds}\frac{ds}{dt} = v\frac{df}{ds} = vf' \tag{2.1}$$

and

$$\ddot{f} = \frac{d}{dt}(\frac{df}{ds}\frac{ds}{dt}) = \frac{d}{ds}(\frac{df}{ds}\frac{ds}{dt})\frac{ds}{dt} = v^2 f'' + f'v\frac{dv}{ds}. \tag{2.2}$$

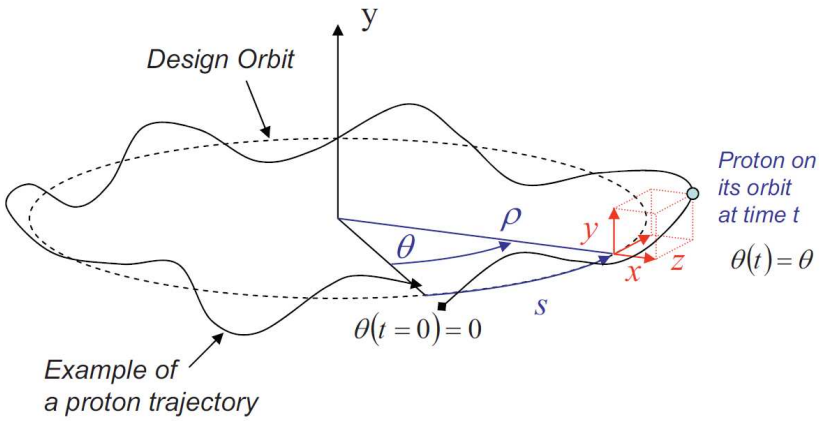

Figure 2.2: Sketch of a proton on a trajectory different from the design orbit [12].

2.2 Single Particle Motion in a Synchrotron

We start from the Lorentz force $\vec{F}$ which describes a single particle motion in a circular accelerator

$$\vec{F} = q(\vec{E} + \vec{v} \times \vec{B}), \tag{2.3}$$

where $q = e$ is the charge of the proton, $\vec{E}$ and $\vec{B}$ are the magnetic and electric fields which act on the particle. We assume that the longitudinal and transverse particle motions can be treated separately. It is easy to justify it if we realize that in the high energy synchrotrons the electric field is used mainly for the longitudinal acceleration and the magnetic field is used mainly for bending, focusing and corrections which act in the transverse plane (we assume $B_s = 0$). We also assume that particle deviations x and y are small in respect to mean accelerator radius ρ and that the transverse velocity $v_\perp$ can be neglected compared to the longitudinal velocity v_s, so $v = \sqrt{v_x^2 + v_y^2 + v_s^2} \approx v_s$. According to those assumptions the Lorentz Force $\vec{F}$ can be decomposed in its longitudinal component F_s and the transverse components F_x and F_y as

$$F_x = e(E_x + v_s B_y), \tag{2.4a}$$

$$F_y = e(E_y - v_s B_x) \tag{2.4b}$$

$$F_s = eE_s. \tag{2.4c}$$

In practice the electric field is not used for steering and focusing the particles in the transverse plane. The reason is that achieving the high enough electric fields is not possible due to the technical constraints. On the other hand, the superconducting magnets of LHC can generate the magnetic field of up to $8\ \mathrm{T}$ which is enough to keep the particles on the design trajectory. Finally the transverse components of the Lorentz force then become

$$F_x = ev_s B_y, \tag{2.5a}$$

$$F_y = -ev_s B_x. \tag{2.5b}$$

Transverse Equations of Motion

Assuming that protons in the LHC are relativistic, we write the relativistic equation of motion for the case without acceleration ($E = 0$)

$$\frac{d}{dt}(m_0 \gamma \vec{v}) = \vec{F} = e\vec{v} \times \vec{B}, \tag{2.6}$$

where m_0 is the rest mass of the proton and γ is the relativistic Lorentz factor. The particle energy and the particle rest mass are constant since the external force is always perpendicular to the proton velocity, so we can write:

$$v_x = \frac{ev_s B_y}{m_0 \gamma}, \tag{2.7a}$$

$$v_y = \frac{-ev_s B_x}{m_0 \gamma}. \tag{2.7b}$$

In the cylindrical coordinates (r, θ, y) (see figure 2.3) the transverse position $\vec{R}$, velocity

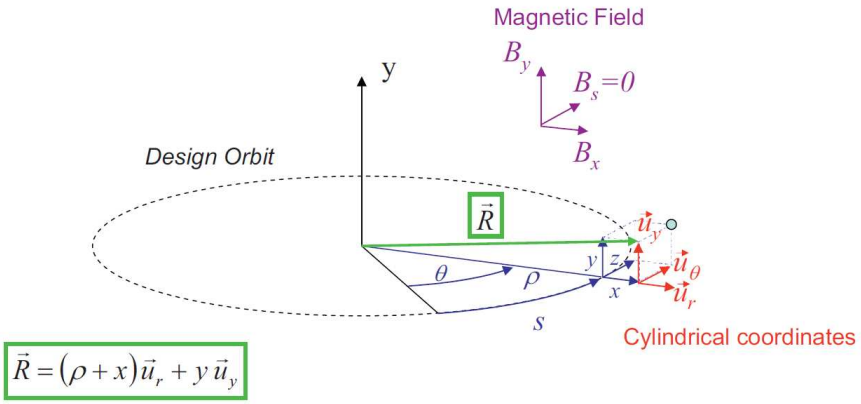

Figure 2.3: Sketch of a proton on a trajectory different from the design orbit [12].

$\vec{V} = \frac{d\vec{R}}{dt}$ and acceleration $\vec{A} = \frac{d\vec{V}}{dt}$ can be expressed as:

$$\vec{R} = r\vec{u_r} + y\vec{u_y}, \tag{2.8a}$$

$$\vec{V} = \dot{r}\vec{u_r} + r\dot{\theta}\vec{u_\theta} + \dot{y}\vec{u_y}, \tag{2.8b}$$

$$\vec{A} = (\ddot{r} - r\dot{\theta}^2)\vec{u_r} + (2\dot{r}\dot{\theta} + r\ddot{\theta})\vec{u_\theta} + \ddot{y}\vec{u_y}. \tag{2.8c}$$

We write the transverse acceleration components:

$$m_0\gamma(\ddot{r} - r\dot{\theta}^2) = ev_sB_y, \tag{2.9a}$$

$$m_0\gamma\ddot{y} = -ev_sB_x. \tag{2.9b}$$

Using $v_s = r\dot{\theta}$, we get

$$m_0\gamma\ddot{r} - \frac{m_0\gamma v_s^2}{r} = ev_sB_y, \tag{2.10a}$$

$$m_0\gamma\ddot{y} = -ev_sB_x. \tag{2.10b}$$

The role of the magnetic field is to keep a proton on the design orbit so the conditions $r = \rho$ and $\ddot{r} = 0$ must be satisfied for a reference particle. We get

$$p_0 = -eB_y^0\rho, \tag{2.11}$$

where $p_0 = m_0\gamma^0 v_s^0$ is the design momentum. The vertical magnetic field B_y^0 is needed to compensate the centrifugal force. The proton momentum $p_0 = m_0\gamma v_s$ can be only increased if the dipole magnetic field strength B_y^0 and/or the bending radius ρ are increased. The equation 2.11 defines the main limitation in building the high energy synchrotrons. In practice the mean radius ρ is constant so the only limitation is in the strength of the magnetic field and it justifies the usage of superconducting magnets in the LHC. We can also write:

$$B_x^0 = 0 \tag{2.12}$$

as no vertical bending is needed on average.

For deviated particles we use $r = x + \rho$, so according to equations 2.10 we get:

$$m_0\gamma\ddot{x} - \frac{m_0\gamma v_s^2}{x + \rho} = ev_sB_y, \tag{2.13a}$$

$$m_0\gamma\ddot{y} = -ev_sB_x. \tag{2.13b}$$

We use the fact that $x \ll \rho$, so

$$\frac{1}{x + \rho} \approx \frac{1}{\rho}\left(1 - \frac{x}{\rho}\right). \tag{2.14}$$

The first order Taylor expansion in x of the vertical magnetic field into a dipolar and quadrupolar magnetic strength gives:

$$B_y = B_y^0 + x\frac{dB_y}{dx} + o(x), \tag{2.15a}$$

$$B_x = y\frac{dB_x}{dy} + o(y). \tag{2.15b}$$

The following equations are then obtained:

$$\ddot{x} + x\left(\frac{v_s^2}{\rho^2} - \frac{ev_s}{m_0\gamma}\frac{dB_y}{dx}\right) = \frac{ev_sB_y^0}{m_0\gamma} + \frac{v_s^2}{\rho}, \tag{2.16a}$$

$$\ddot{y} + y\frac{ev_s}{m_0\gamma}\frac{dB_x}{dy} = 0. \tag{2.16b}$$

The time variable t can be replaced by the curvilinear variable $s = vt$. Using $\ddot{x} = v_s^2x'', x'' = \frac{d^2x}{ds^2}$ as there is no longitudinal acceleration we have

$$x'' + x\left(\frac{1}{\rho^2} - \frac{e}{m_0\gamma v_s}\frac{dB_y}{dx}\right) = \frac{eB_y^0}{m_0\gamma v_s} + \frac{1}{\rho}, \tag{2.17a}$$

$$y'' + y\frac{e}{m_0\gamma v_s}\frac{dB_x}{dy} = 0. \tag{2.17b}$$

Considering the vacuum region inside the magnet in the absence of the electrical currents and fields one yields from the Maxwell equations $\vec{\nabla} \times \vec{B} = 0$. We assumed that $B_s = 0$, so we have in particular $\frac{dB_x}{dy} = \frac{dB_y}{dx} = g$ which is the transverse magnetic field strength gradient. If we use $p \approx p_s = m_0\gamma v_s$, we get:

$$x'' + x\left(\frac{1}{\rho^2} - \frac{eg}{p}\right) = \frac{eB_y^0}{p} + \frac{1}{\rho}, \tag{2.18a}$$

$$y'' + y\frac{eg}{p} = 0. \tag{2.18b}$$

According to equation 2.11 $\frac{eB_y^0}{p} = -\frac{1}{\rho}$, so the right side of the equation 2.18a vanishes. Additionally we define the quadrupole strength $k = \frac{eg}{p_0}$, so we obtain the transverse equations of motion for a proton in a circular accelerator in the linear approximation

$$x'' + x\left(\frac{1}{\rho^2} - \frac{eg}{p}\right) = 0, \tag{2.19a}$$

$$y'' + y\frac{eg}{p} = 0. \tag{2.19b}$$

Equation 2.19 holds only if we consider a local part of an accelerator with a local radius of curvature $\rho(s)$ and a local focusing strength $k(s)$. In the more general case, the equations of motion in both planes can be written as Hill's equations

$$x'' + K_h(s)x = 0, \tag{2.20a}$$

$$y'' + K_v(s)y = 0. \tag{2.20b}$$

with $K_h(s) = \frac{1}{\rho(s)^2} - k(s)$ in the horizontal plane and $K_v(s) = k(s)$ in the vertical plane.

Solution of the Hill's Equations of Motion

In this paragraph we use z as a general coordinate that can be either x (horizontal) or y (vertical). The general solution of the homogeneous Hill's equation of motion (equation 2.20) is

$$z(s) = \sqrt{\tilde{\varepsilon_z}}\sqrt{\beta_z(s)}cos\left(\psi_z(s) + \phi_z^0\right), \tag{2.21a}$$

$$z'(s) = -\frac{\sqrt{\tilde{\varepsilon_z}}}{\sqrt{\beta_z(s)}}\left[\alpha_z cos\left(\psi_z(s) + \phi_z^0\right) + sin\left(\psi_z(s) + \phi_z^0\right)\right], \tag{2.21b}$$

where $\beta_z(s)$ is the beta function and

$$\psi_z(s) = \int_{\hat{s}=0}^{s} \frac{1}{\beta_z(\hat{s})} d\hat{s} \tag{2.22}$$

is the phase advance. We also define

$$\alpha_z(s) = -\frac{\beta_z'(s)}{2}. \tag{2.23}$$

$\hat{\varepsilon_z}$ and ψ_z^0 are constants defined by the initial conditions. The steps to obtain this solution using the Floquet theorem can be found in ref. [11].

2.3 Transverse Emittance Definition

In this paragraph we will define the transverse beam emittance.

Using the equations 2.21a and 2.21b the following equation can be obtained

$$\frac{1}{\beta_z(s)}\left[z^2(s) + \beta_z(s)z'(s) + \alpha_z(s)z(s)\right] = \hat{\varepsilon_z}. \tag{2.24}$$

Defining the parameter $\gamma_z(s)$

$$\gamma_z(s) = \frac{1 + \alpha_z^2(s)}{\beta_z(s)} \tag{2.25}$$

we can write:

$$\gamma_z(s)z^2(s) + 2\alpha_z(s)z(s)z'(s) + \beta_z(s)z'^2(s) = \hat{\varepsilon_z}. \tag{2.26}$$

Equation 2.26 is the implicit equation of an ellipse of constant area $\pi\hat{\varepsilon_z}$ in the phase space plane (z, z'). Along the design orbit, the shape of the ellipse may vary, but its area remains $\hat{\varepsilon_z}$. An ensemble of protons injected in a machine has a distribution of initial amplitudes z and angles z'. This initial phase space distribution can be characterized by its beam size $\sigma_z(0)$, and its beam divergence $\sigma_z'(0)$. Along the accelerator, each proton therefore traces an ellipse of a different area $\hat{\varepsilon_z}$ in the (z, z') phase space. The 63% transverse emittance $\varepsilon_z^{63\%}$ is defined by the phase space ellipse that contains 63% of the ellipse trajectories of all protons (see figure 2.4). In addition, in the case of an unperturbed uncoupled unaccelerated proton r.m.s. transverse emittance ε_z is a

constant of motion and depends only on the initial transverse beam size $\sigma_z(0) = \sqrt{\varepsilon_z \beta_z(0)}$ and divergence $\sigma'_z(0) = \sqrt{\varepsilon_z \gamma_z(0)}$. The transverse r.m.s. beam size $\sigma_z(s)$ and beam divergence $\sigma'_z(s)$ along the accelerator are given by

$$\sigma_z(s) = \sqrt{\varepsilon_z \beta_z(s)}, \tag{2.27a}$$

$$\sigma'_z(s) = \sqrt{\varepsilon_z \gamma_z(s)}. \tag{2.27b}$$

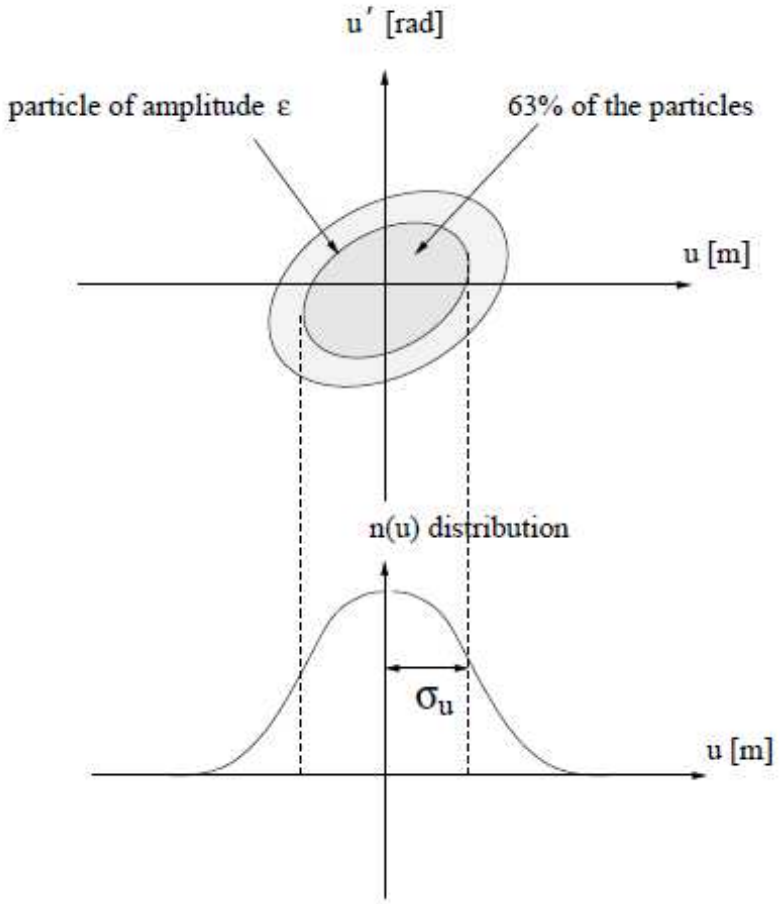

Figure 2.4: Definition of $\varepsilon_z^{63\%}$ beam emittance and beam profile [14].

In the case of an accelerated protons the transverse emittance is not a constant of motion. Instead, the normalized emittance

$$\varepsilon_N = \varepsilon \beta \gamma, \tag{2.28}$$

(β, γ are relativistic Lorentz factors) is conserved according to the Liouville theorem. It means that the transverse beam size changes with energy.

Such defined transverse beam emittance is a matter of measurements in the Beam Gas Ionization monitors. It is important to know the beam emittance for the luminosity estimation and beam diagnostics reasons. Luminosity is a beam parameter which indicates the ability of

a particle accelerator to produce the required number of interactions in head collision. It is inversely proportional to the beam size in the collision location. As the beam size cannot be measured at the collision point, it is measured elsewhere and the beam emittance is calculated. The emittance is supposed to be constant around the ring and therefore allows to relate a beam size measurement done at any location of the ring to the beam size at the interaction point.

From the beam diagnostics point of view it is important to know whether the emittance is really constant. In spite of the Liouville theorem, there are many phenomena that may affect the emittance. A few examples are listed below:

- coupling between degrees of freedom;
- intra-beam scattering;
- scattering on residual gas;
- synchrotron radiation emission;
- wake fields;
- space charge effects;
- beam-beam effects.

The emittance measurements help to identify and reduce those phenomena.

Chapter 3

The BGI Data Analysis

The Beam Gas Ionization monitor was design mainly for ion beams with transverse emittances of about $3.5\ \mu\mathrm{m}$ and bunch charge of about 10^{10}. Soon after LHC start the emittances reached much smaller values, even of $0.5\ \mu\mathrm{m}$ resulting in much smaller beams. It also turned out that BGI registers a clear signal from proton beam, which are a main matter of interest in LHC, but they intensities are larger than in case of ions and reach $1.5 \cdot 10^{11}$ charges per bunch. In these conditions the measurements suffer from unforseen effects discussed more in next chapters.

The BGI also operates in extreme conditions in terms of the vacuum requirements, high voltage, radiation and many more. The beam profile measurements are therefore complex and many factors influence on the registered data. The procedure of obtaining the beam size and the comparison with another instrument will be presented in this chapter.

3.1 The BGI Data

As described in the section 1.3 the Beam Gas Ionization monitor registers the beam profile as the camera image. The image is then digitized (see picture 3.1) and a series of operations is performed:

1. cleaning from noise (by threshold);
2. correcting for nonuniform MCP gain;
3. correcting for camera tilt;
4. masking noisy areas.

Projection on horizontal axis is done at the end. It contains the beam profile together with remaining camera noise and other artifacts. The Gaussian parametrization is used to obtain the profile width. To improve this procedure, tails dominated by noise are not taken into the fit

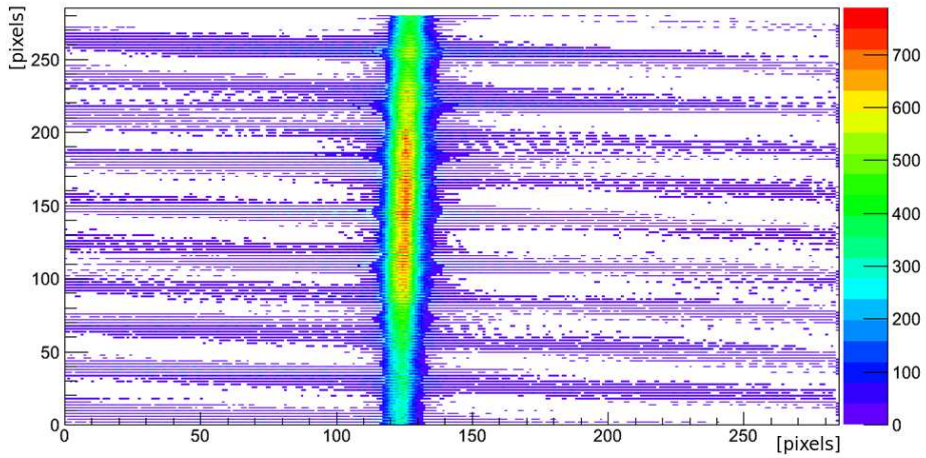

Figure 3.1: The example image of the beam taken by the vertical BGI monitor.

range so only the central part of the profile is fitted (see figure 3.2). At the end the σ obtained from the fit is multiplied by a pixel calibration factor, which is 0.11 mm.

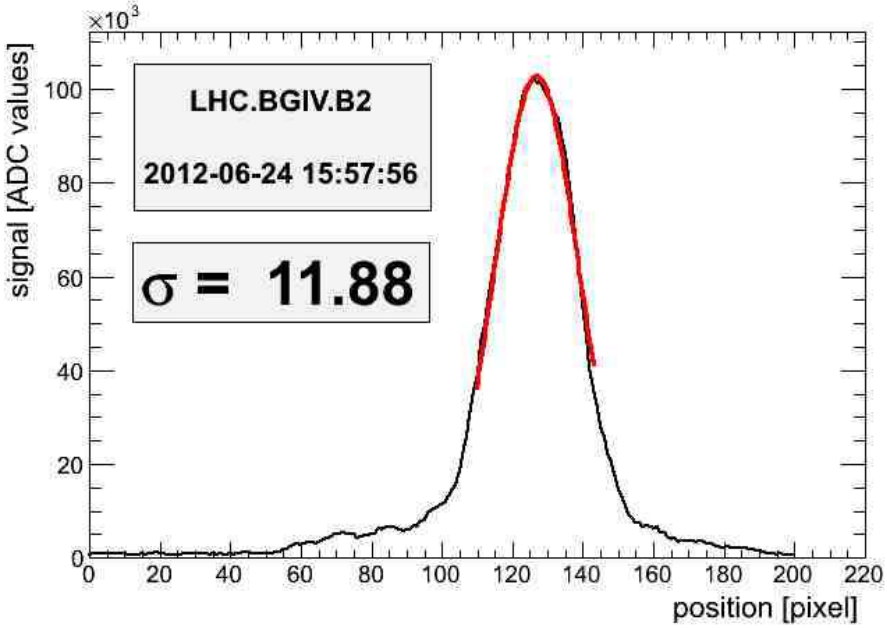

Figure 3.2: Gaussian fit to the beam profile. Tails dominated by noise are not taken into the fit range.

3.2 Cross-calibration with the Wire Scanner

There are many ways to calibrate the BGI and make sure that the obtained results are correct. The most complete one is comparison of BGI measurements with Wire Scanner.

Except of BGI, there are two other emittance measuring devices in LHC: the Synchrotron Radiation monitor (BSRT) and the Wire Scanner (WS). The Synchrotron Radiation monitor, which profits from the synchrotron light emitted by the slightly deviated beam, itself requires the calibration with the Wire Scanner [15] so it should not be used for the comparison with the BGI. Therefore, the Wire Scanner is used for the comparison.

The WS measures the transverse beam profile with use of a $30\ \mu\mathrm{m}$ carbon wire which crosses the beam. As the wire passes through the beam, the cascade of secondary particles is generated and registered by scintillation detectors in order to obtain the beam profile. The scheme of the Wire Scanner operation principle is sketched on figure 3.3.

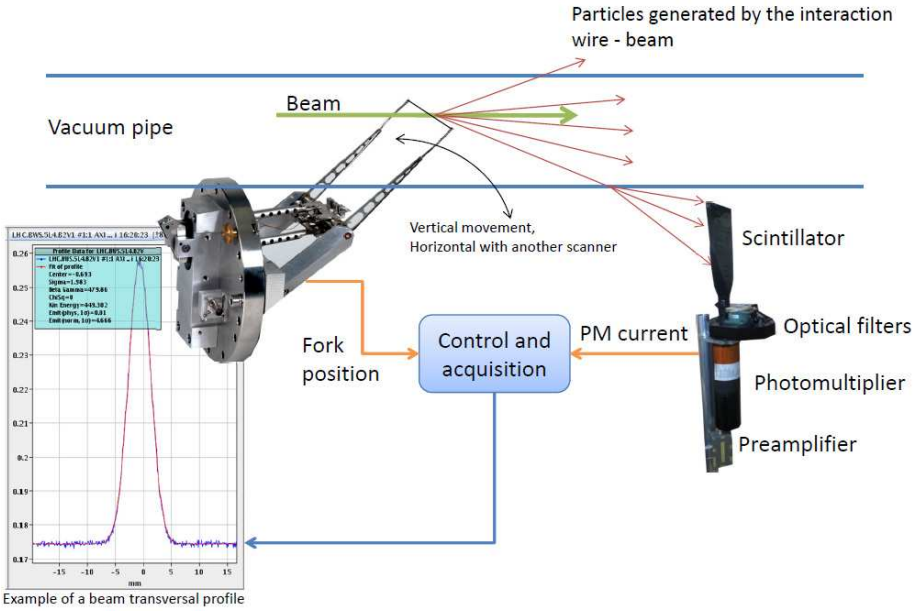

Figure 3.3: Sketch of the Wire Scanner operation principle [16].

Use of the Wire Scanner is limited to the low intensity LHC beams. The reason is that a high brightness (number of particles per cross section), dense beam destroys the wire. Therefore only about 2% of nominal intensity beam can be measured with WS. On the other hand the Beam Gas Ionization monitor requires higher intensity to ensure enough signal from gas ionization. Therefore, in case of a proton beam, the comparison of BGI with WS is complicated or even impossible.

Fortunately LHC is used not only for acceleration of protons but also lead ions. An ion beam is normally less intense in terms of number of particles than a proton beam so it does not break the wire even at the top LHC energy ($4\ \mathrm{ZTeV}$). At the same time the intensity of a

lead beam expressed as a number of charges is sufficient to give a clear signal in BGI even at injection energy (450 ZTeV). The cross section for ionization process scales with the number of charges in square, so lead ions interact with a gas much more likely than protons. Therefore the comparison was possible for a lead beam.

The BGI and WS are located in different locations around the ring. In order to compare profiles obtained by both instruments a scaling of the profile with an optical β function must be done. In figure 3.4 a comparison of the beam profiles is presented at injection and top LHC energy. The β functions used for a scaling are shown in table 3.1.

B2V	**WS**	**BGI**
injection energy	418.95 m	217.19 m
top energy	451.04 m	225.35 m

Table 3.1: Optical β functions for WS and BGI.

The comparison shows that for injection energy the profiles of WS and BGI correspond very well to each other but for the top energy the BGI profile is significantly larger than the WS profile. Observations suggest that this effect is even stronger for a proton beams. The possible justification will be presented in the next chapters.

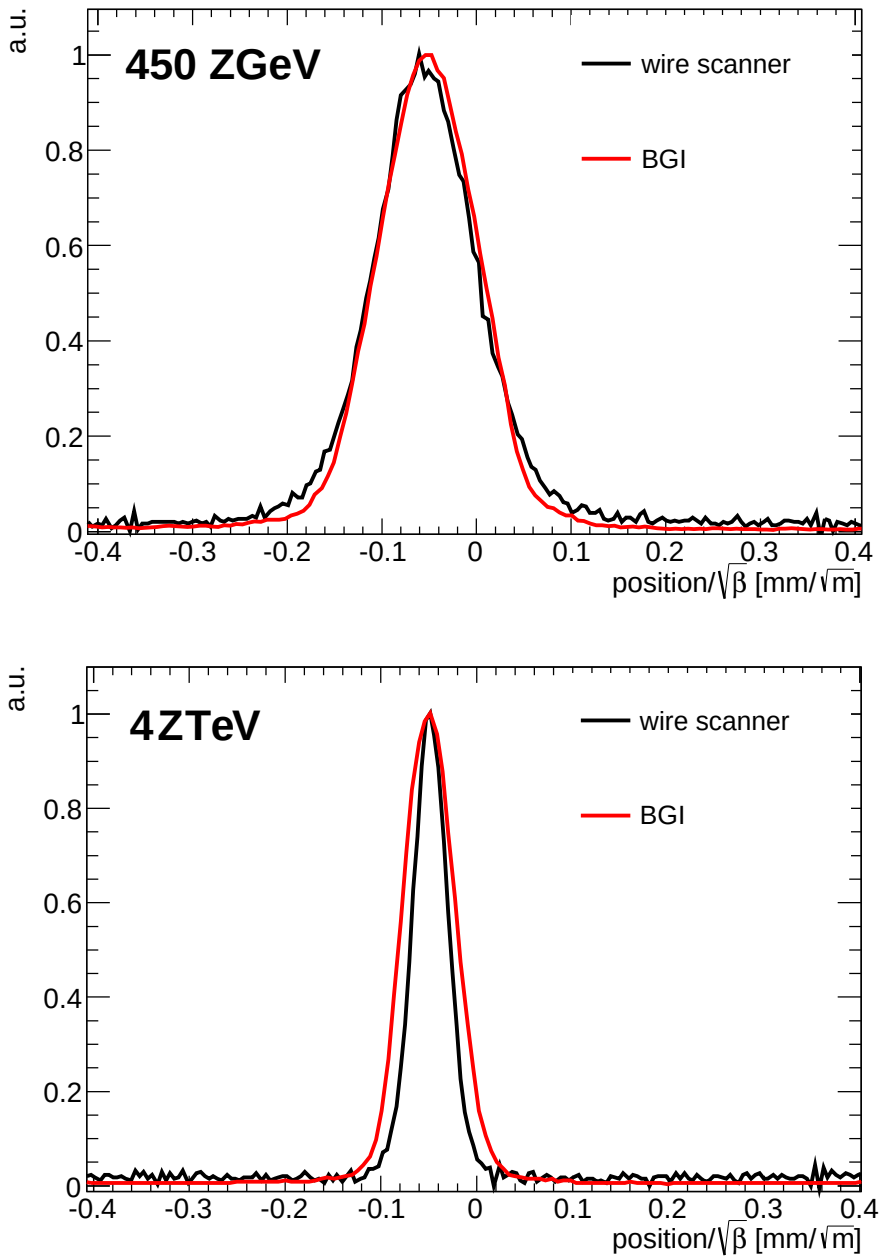

Figure 3.4: Comparison of beam profiles in WS and in BGI at the injection (450 ZGeV) and at top (4 ZTeV) energy.

Chapter 4

Simulation description and results

In chapter 3 it was shown that the profile of a beam measured by the Beam Gas Ionization monitor is wider in comparison to the Wire Scanner measurement. We suspect that two effects can be responsible for this observation:

1. larger than expected initial velocities of electrons,
2. electron interaction with bunch charge – so called space charge effect.

The simulations have been done to check these effects.

4.1 Simulation Description

4.1.1 PyECLOUD simulation

The PyECLOUD code, written in CERN for the simulations of the electron cloud build-up in the particle accelerators, has been adapted by the authors so that it can be used to determine the electron trajectories in the presence of the proton beam and the external fields. The technical details about the code can be found in [17]. Its algorithm is listed below:

- protons grouped into macroparticles are placed in bunch according to input parameters (Gaussian distribution). See table 4.1;
- bunch goes through the ”window” of given length, where the electron movement is calculated;
- in each time-step we consider only protons which are inside the ”window”;
- electrons are generated inside the ”window” in the position of protons;
- electrons move according to the electric field of protons and to the external electric and magnetic fields;

- in each time-step we consider newly generated electrons and all the electrons from the previous steps;
- electron position on x-axis is registered when it hits the surface (4 cm below the bunch center) (corresponding to MCP);
- electron position fills the histogram.

The simulation input parameters can be found in the table 4.1. The numeric simulation parameters are listed in table 4.2. Figure 4.1 shows the example result obtained from the simulation.

Parameter name	**Value**
Beam energy (protons)	$\mathrm{E_{beam}} = 450 - 7000$ GeV
Beam energy (lead ions)	$\mathrm{E_{beam}} = 450 - 7000$ ZGeV
Chamber electric field	$\mathrm{E} = \frac{4000\mathrm{V}}{8.5\mathrm{cm}}$
Chamber magnetic field	$\mathrm{B} = 0.2$ T
Beam intensity (protons)	$\mathrm{I} = 1.1 - 1.65 \cdot 10^{11} \frac{\mathrm{protons}}{\mathrm{bunch}}$
Beam intensity (lead ions)	$\mathrm{I} = 1.0 \cdot 10^{10} \frac{\mathrm{charges}}{\mathrm{bunch}}$
Horizontal emittance	$\varepsilon_{\mathrm{x}} = 1.0 - 4.5\ \mu$m
Vertical emittance	$\varepsilon_{\mathrm{y}} = 1.0 - 4.5\ \mu$m
Bunch length (4σ)	$\sigma_{\mathrm{z}} = 1.0 - 1.5$ ns

Table 4.1: Simulation input parameters.

Parameter name	**Value**
Simulation length	$\mathrm{t_{max}} = 10$ ns
Time step	$\mathrm{dt} = 50$ fs
Number of macroparticles	$\mathrm{N_{MP}} = 10^5$
Grid size of the beam	$\mathrm{L} = 40\ \mu$m
Profile bin size	$\mathrm{d} = 10\ \mu$m

Table 4.2: Simulation numeric parameters.

4.1.2 Geant4 simulation

The electrons liberated in the ionization process have some initial momentum which affects their trajectories and therefore the overall beam profile. PyECLOUD code does not include

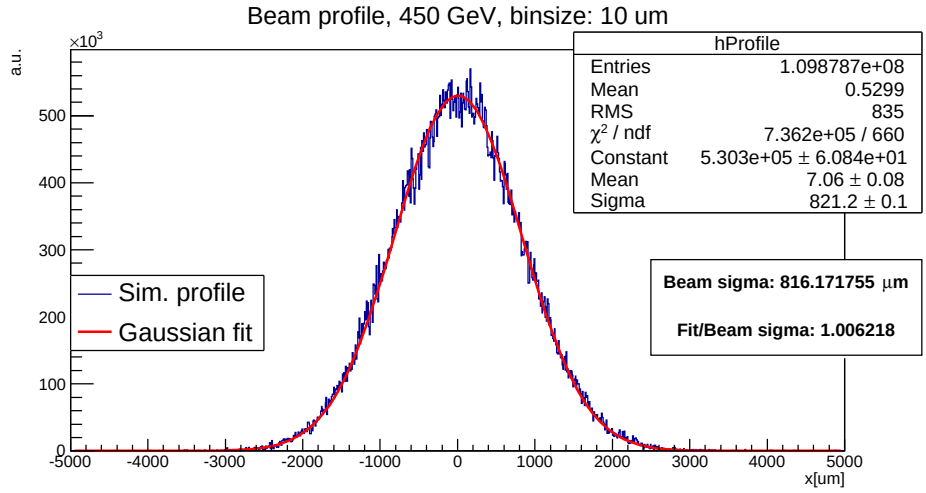

Figure 4.1: Profile of 450 GeV beam obtained by tracking the liberated electrons (histogram) and a Gaussian fit.

the ionization process: the electrons are randomly (according to the proton distribution of the beam) generated. To overcome this problem the Geant4 [18] simulation code is used to obtain the initial electron momentum distribution.

The simulation setup is very simple: a simple proton of energy between $450\ \mathrm{GeV}$ to $7000\ \mathrm{GeV}$ travels through the `G4Box` object filled with a low density Neon gas. The ionization process is included into the physics list and the cuts for electromagnetic processes were set as low as $30\ \mathrm{eV}$ in order to account for contribution from very low energy transfers. Additionally the multiple scattering process is replaced by a single scattering because of the low gas density. As the result of the Geant4 simulations the electron initial momentum distribution was obtained, see figures 4.2 and 4.3. The PyECLOUD initial momenta of the electrons are generated according to those distributions. One can see that electrons are generated forward but the momentum transfer in transverse direction is much larger than along the beam. This is caused mainly due to relativistic contraction of the projectile electric field in the beam direction. This phenomenon was studied e.g. in [19].

The mean absolute value of the electron momentum is of around $7\ \mathrm{keV/c}$ in the transverse direction and around $0.4\ \mathrm{keV/c}$ in longitudinal direction. As the electrons in the PyECLOUD simulation are subjected to the constant magnetic field of $0.2\ \mathrm{T}$ oriented in y direction, the initial momentum causes the electrons to follow the helix trajectory with a gyroradius of around $110\ \mu\mathrm{m}$. This value is close to the typical beam size value at energy of $7\ \mathrm{TeV}$ what was the first indication of inssuficient value of used magnetic field. Figure 4.4 presents the electrons gyroradius dystribution and integrated dystribution.

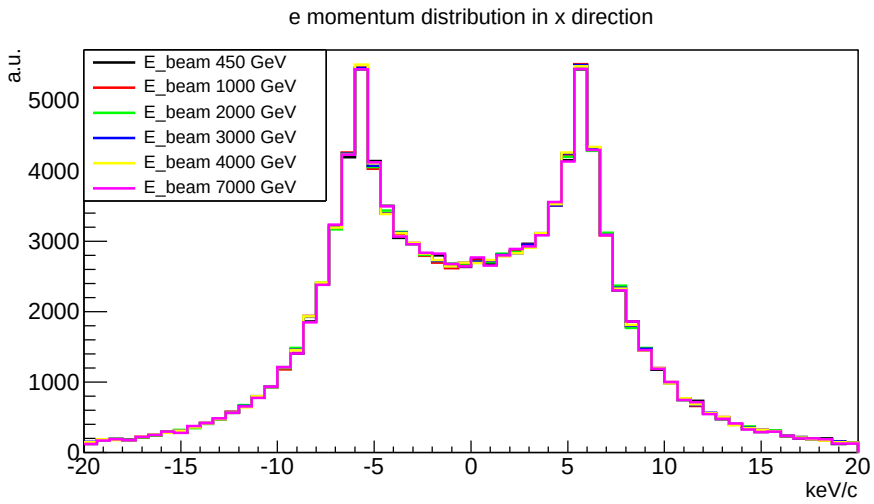

Figure 4.2: Electron initial momentum distribution in the transverse direction. It does not depend on the impacting proton energy. The mean of the absolute value is around $7\ \mathrm{keV/c}$.

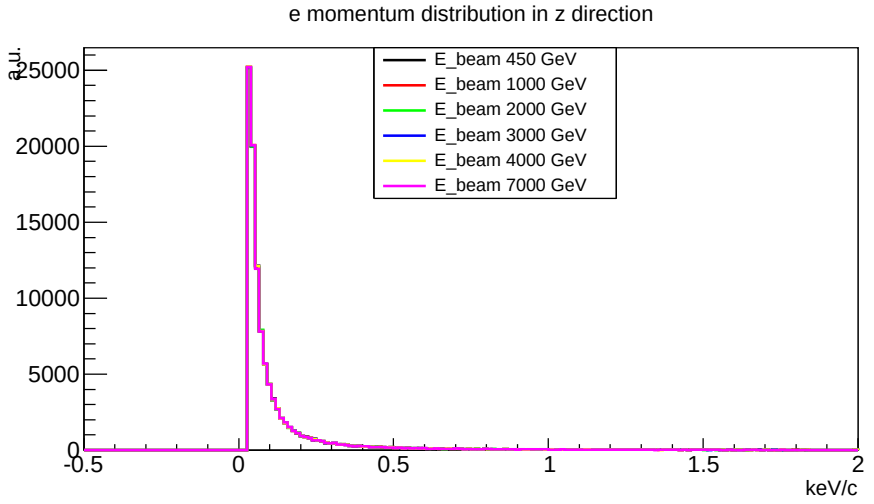

Figure 4.3: Electron initial momentum distribution longitudinal plane. It does not depend on the impacting proton energy. The mean of the absolute value is around $0.4\ \mathrm{keV/c}$.

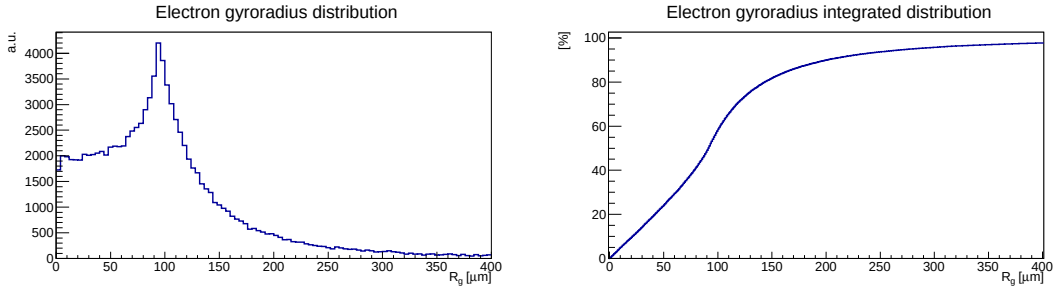

Figure 4.4: Electrons gyroradius dystribution (left) and integrated dystribution (right).

The justification for taking into account the electron initial momenta is shown on figure 4.5. The two upper plots shows the beam profiles when the electron initial momentum is included

and the two bottom plots show the beam profiles for the electrons produced at rest.

The are two conclusions coming from those plots. The first is that the low energy beam only slightly affect the electron trajectories, so the electron profile directly corresponds to the beam profile. The second is that electron initial momentum is relevant and has to be taken into account. The bottom right plot shows the strange shape of the beam profile which is far from the profiles observed in the BGI monitors. The upper right plot shows the profile close to Gaussian which refers to the profiles seen in the BGI monitors. The non-Gaussian contribution to this profile is the result of the space charge effects which appear for a dense, high energy beam. This issue will be discussed in the next section.

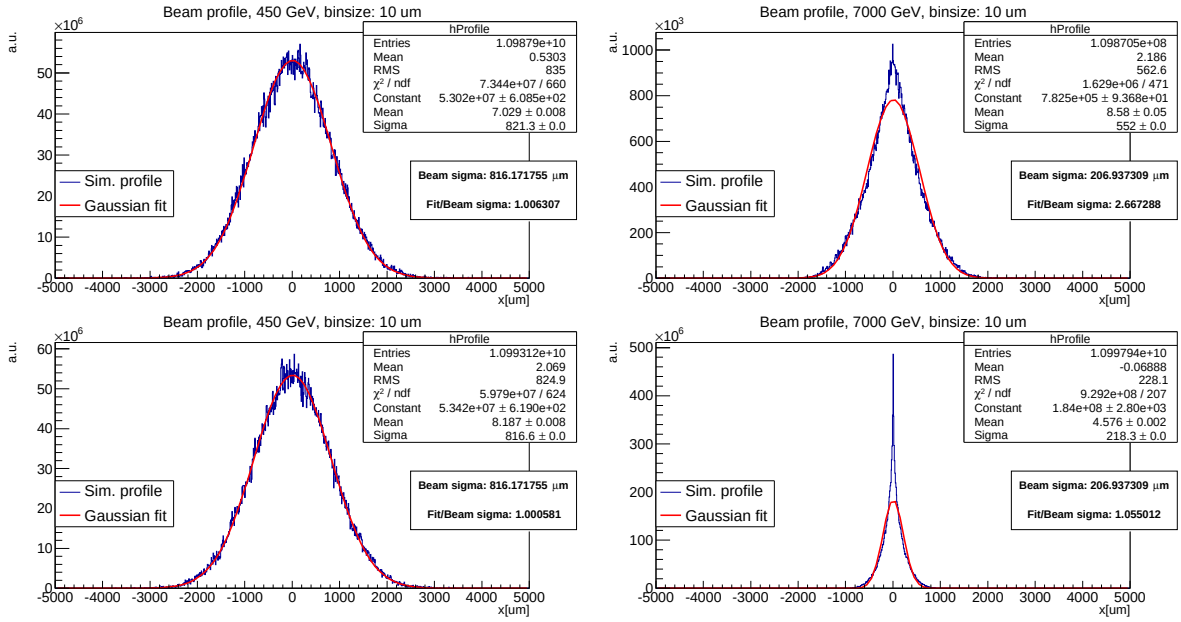

Figure 4.5: The two upper plots correspond to the case when the electron initial momentum is included. The two bottom plots show the profiles in case of the electrons produced at rest.

4.2 Simulation results

Before showing the results, the beam space charge will be defined and its possible impact on beam profile will be discussed.

In our case the space charge effect refers to the interactions between electrons liberated by the gas ionization and protons of the beam, where those protons are not treated separately but as a continuum. This effect is complex as a beam can consist of around 10^{11} protons distributed in space and the electrons move through this space. As the result, electrons obtain extra momentum which affect their trajectories and increase the gyroradius. This can lead to overall profile broadening and deviation, which will be presented in this section.

4.2.1 Profiles Broadening

By running the simulations it was found that the obtained profiles width is larger than the width of the simulated beams. It was observed that this broadening is negligible for the low energies and increases during the energy ramp. Additionally the profiles loose their Gaussian shape. The figure 4.6 show those effect for several energies.

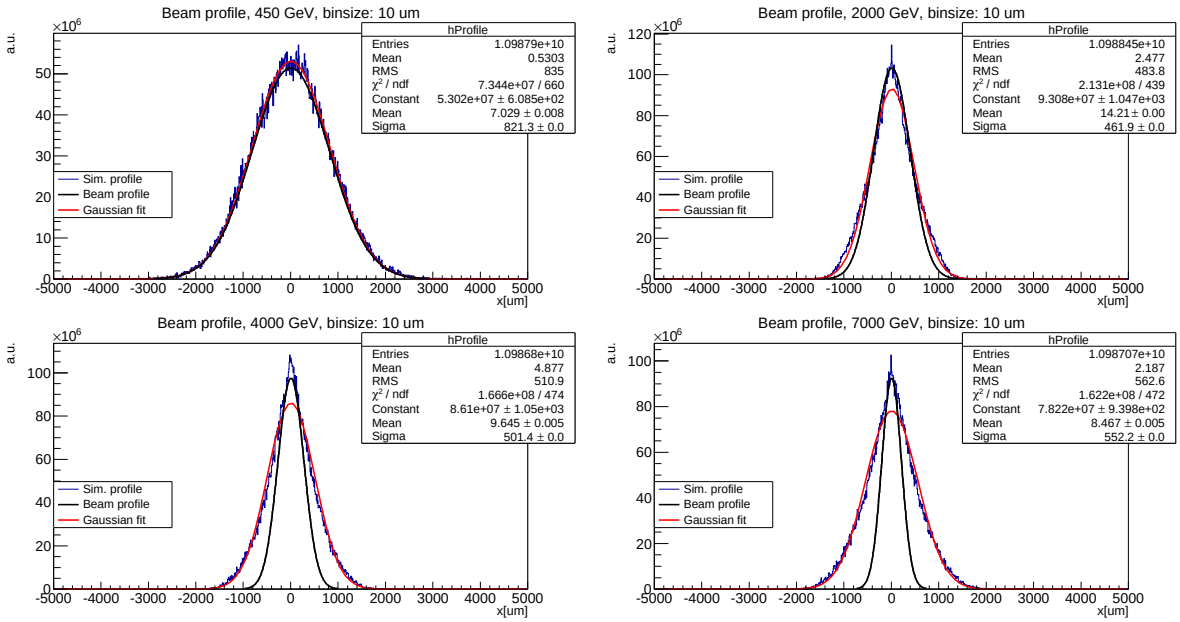

Figure 4.6: The profile broadening for several beam energies. The blue curve refers to the beam width.

4.2.2 Emittance Plots for the Energy Ramp

As it was shown in the section 2.3 the normalized emittance is conserved during the energy ramp if no perturbation occur. The relation between the normalized and physical emittance is

$$\varepsilon_N = \varepsilon\beta\gamma, \tag{4.1}$$

where β and γ are the relativistic Lorentz factors. For the high energy LHC beams $\beta \approx 1$, so we get

$$\varepsilon_N = \varepsilon\gamma. \tag{4.2}$$

The physical beam size depends on the physical emittance

$$\sigma = \sqrt{\varepsilon\beta} = \sqrt{\frac{\varepsilon_N\beta}{\gamma}}, \tag{4.3}$$

so the beam size decreases during the energy ramp. This leads to an increase of the charge density inside the beam which enhances the space charge effects.
In the rest of this chapter *emittance* refers to the *normalized emittance* unless it is written explicitly.

The emittance obtained from the simulated profiles width is plotted on the figures 4.7 – 4.9. It is easy to see that the profile broadening presented on the figure 4.6 causes a significant increase of a measured emittance.

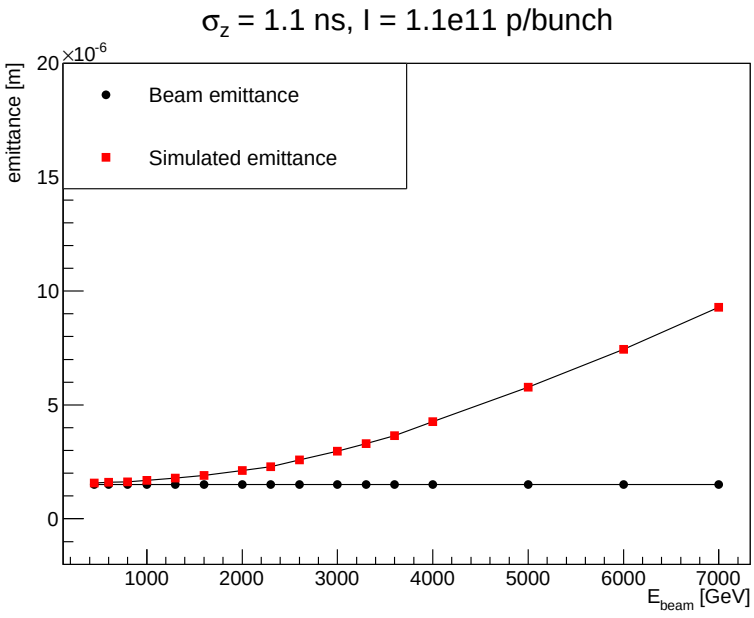

Figure 4.7: Emittance as a function of energy, for a bunch intensity of $1.1 \cdot 10^{11}$.

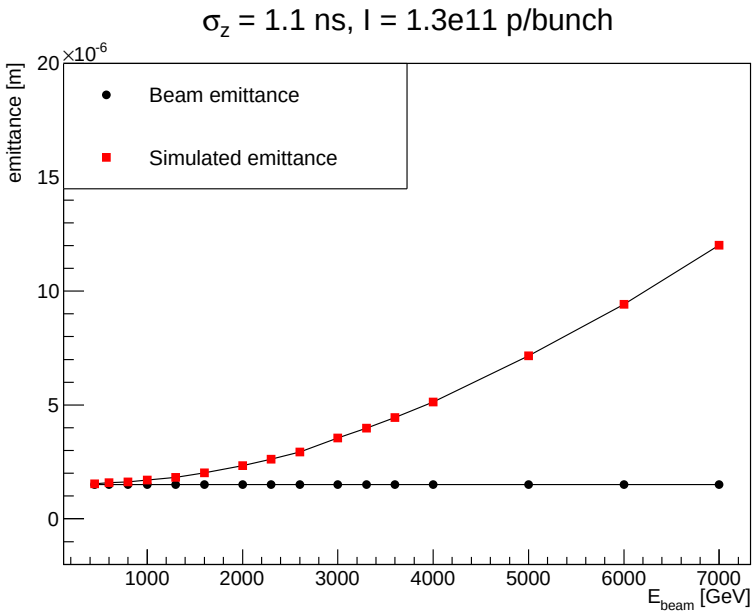

Figure 4.8: Emittance as a function of energy, for a bunch intensity of $1.3 \cdot 10^{11}$.

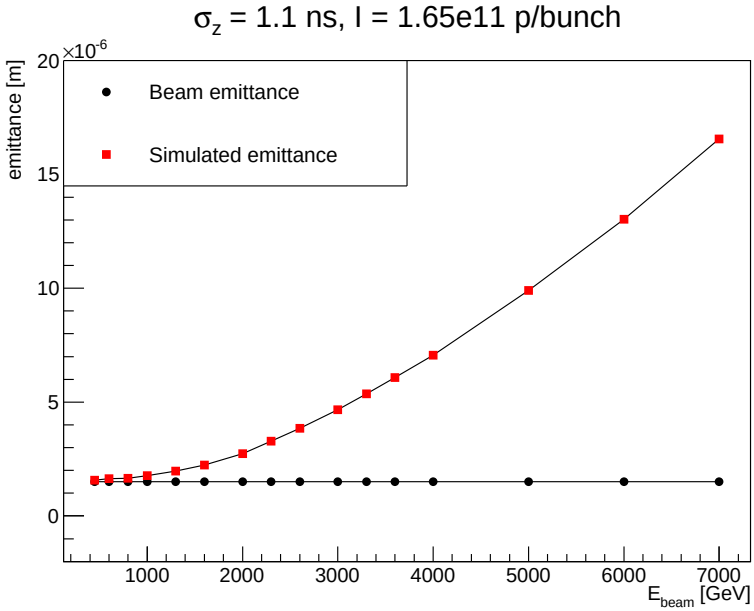

Figure 4.9: Emittance as a function of energy, for a bunch intensity of $1.65 \cdot 10^{11}$.

Electric and Magnetic Field Variation

It was checked how the increase of the electric or magnetic field in the chamber impacts on the broadening effect. The emittance plot (see figure 4.10) obtained from the simulations with the chamber electric field of $\frac{10000V}{8.5cm}$ shows that an increase of the electric field does not remove the broadening effect. Increasing the magnetic field from 0.2 T to 1 T shows that the increase of the emittance is largely reduced, see figure 4.11. The results are consistent for any beam considered in LHC, the broadening problem could be solved by increasing the magnetic field to 1 T.

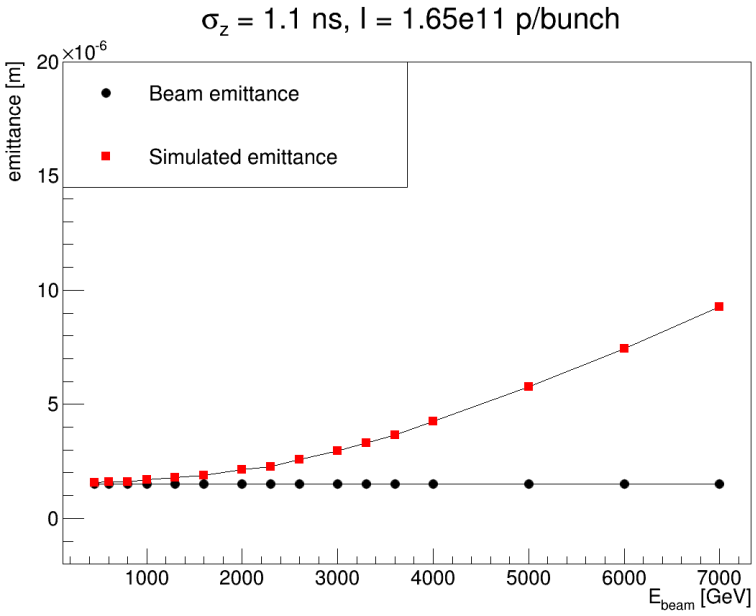

Figure 4.10: Emittance as a function of energy for E = $\frac{10000V}{8.5cm}$.

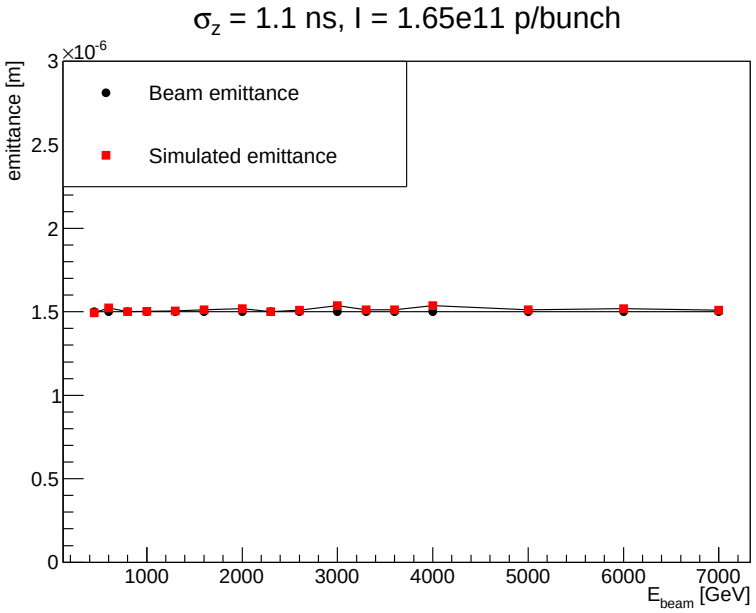

Figure 4.11: Emittance as a function of energy for $\mathrm{B} = 1\ \mathrm{T}$.

4.2.3 The simulations of the lead beam

The simulations of a proton beam cannot be compared with the BGI measured data because as described in chapter 3 the calibration with another instrument cannot be performed and therefore the data are not reliable. The simulations of the lead beam were done to check the results with the instrument data.

In September 2012 during the lead ions beam run the beam profile was measured both by the Wire Scanner and the Beam Gas Ionization monitor. The comparison of the results was presented on figure 3.4. Table 4.3 summarizes the obtained beam profile widths when the optical β_{BGI} function in the location of BGI was taken into account. It shows a good agreement for beam energy of 450 ZGeV but for the energy of 4000 ZGeV the profile obtained by BGI is clearly wider.

B2V	**WS**	**BGI**
injection energy	807 μm	772 μm
top energy	280 μm	405 μm

Table 4.3: Beam profiles widths obtained by WS and BGI.

Table 4.4 contains the parameters of the simulated lead beam which refers to the real beam parameters. The results of the simulations are presented on figures 4.12 and 4.13. The profiles widths which result from the simulations correspond very well to the Wire Scanner data and differ from the BGI data. It might mean that the BGI monitor has some detector effects which influence the measurements. The possible explanations are listed below:

- camera tilt underestimation,
- beta-beat,
- beam oscillations,
- PSF due to the initial gyroradius.

For now, there is no alignment procedure for the BGI cameras. It was calculated that for such a small beam a misalignment of 2 degrees can be a source of the profile broadening seen on the figure 3.4 and in the table 4.3.

It seems that for the ion beam and considered intensity the space charge effects do not play a role. The small profile broadening which is present on figure 4.13 is probably caused by the electron gyroradius which is calculated to be around 120 μm.

Parameter name	Injection energy	Top energy
Beam energy	$\mathrm{E_{beam}} = 450$ ZGeV	$\mathrm{E_{beam}} = 4000$ ZGeV
Chamber electric field	$\mathrm{E} = \frac{4000\mathrm{V}}{8.5\mathrm{cm}}$	$\mathrm{E} = \frac{4000\mathrm{V}}{8.5\mathrm{cm}}$
Chamber magnetic field	$\mathrm{B} = 0.2$ T	$\mathrm{B} = 0.2$ T
Beam intensity	$\mathrm{I} = 1.0 \cdot 10^{10} \frac{\mathrm{charges}}{\mathrm{bunch}}$	$\mathrm{I} = 1.0 \cdot 10^{10} \frac{\mathrm{charges}}{\mathrm{bunch}}$
Horizontal emittance	$\varepsilon_\mathrm{x} = 0.57\ \mu$m	$\varepsilon_\mathrm{x} = 0.59\ \mu$m
Vertical emittance	$\varepsilon_\mathrm{y} = 0.57\ \mu$m	$\varepsilon_\mathrm{y} = 0.59\ \mu$m
Horizontal β function	$\beta_\mathrm{x} = 217.19$ m	$\beta_\mathrm{x} = 225.35$ m
Vertical β function	$\beta_\mathrm{y} = 217.19$ m	$\beta_\mathrm{y} = 225.35$ m
Bunch length (4σ)	$\sigma_\mathrm{z} = 1.22$ ns	$\sigma_\mathrm{z} = 1.25$ ns

Table 4.4: Simulation input parameters.

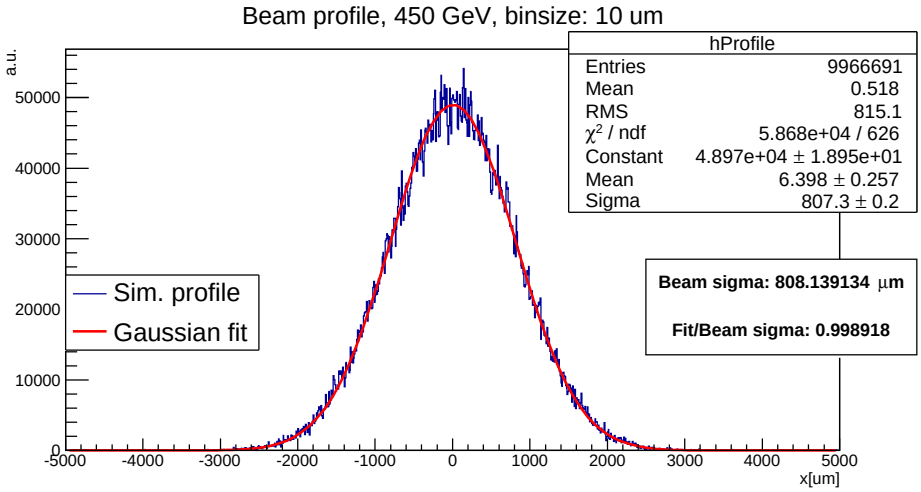

Figure 4.12: Simulated profile of a lead ions beam for the energy of 450 ZGeV.

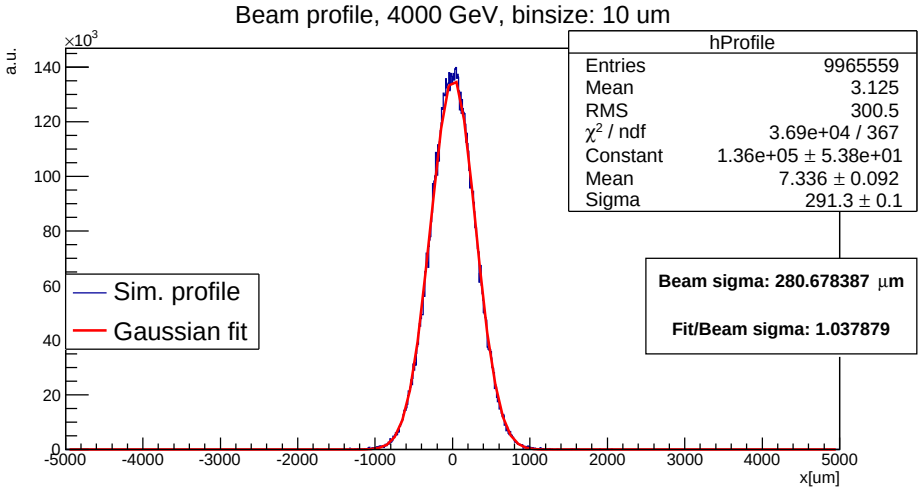

Figure 4.13: Simulated profile of a lead ions beam for the energy of 4000 ZGeV.

Chapter 5

Magnetic field threshold in the BGI electron dynamics

The simulation results clearly show that the space charge effects of a dense, proton beam affect the spatial distribution of the liberated electrons in BGI and therefore the instrument cannot deliver reliable measurements. It was also found that a high magnetic field can be used to ensure a correct operation of the instrument. The investigation of the minimal magnetic field required to dump the space charge effects of a beam of given parameters will be presented in this chapter. The theoretical predictions, presented below, were made by Giuliano Franchetti[1] who participated in this research.

5.1 Electrons dynamics in a uniform filled bunch

We assume the bunch of particles to be a cylinder of length σ_z and radius σ_r uniformly filled with protons. The electric field of the space charge is then $\mathbf{E_{sc}} = (E_{sc,x}, E_{sc,y}, E_{sc,z})$. The electrons are also subjected to the magnetic field of the BGI magnet $\mathbf{B} = (B_x, B_y, B_z)$ and the electric field of the BGI $\mathbf{E} = (E_x, E_y, E_z)$.

If we neglect the interaction between the electrons, the motion of one electron will be given by the Lorentz force

$$\frac{d}{dt} m\gamma \mathbf{v} = -e\left(\mathbf{E} + \mathbf{E_{sc}}\right) - e\mathbf{v} \times \mathbf{B}, \tag{5.1}$$

where m is the mass of the electrons produced by the ionization of the rest gas, and $\gamma = 1/\sqrt{1 - (\mathrm{v/c})^2}$.

We assume the $x - y - z$ reference frame, where z is the beam direction and y axis is vertical, so the fields get the form: $\mathbf{B} = (0, B, 0)$, $\mathbf{E} = (0, E, 0)$ and $\mathbf{E_{sc}} = (\alpha_x x, \alpha_y y, \alpha_z z)$, where $\alpha_x = \alpha_y, \alpha_z > 0$ are directly proportional to the number of protons in the bunch. In this notations the center of the bunch is placed on the origin of the axes.

[1] email: g.franchetti@gsi.de

The components of the equations of motion are:

$$\frac{d}{dt}m\gamma v_x = -e\alpha_x x + ev_z B, \tag{5.2a}$$

$$\frac{d}{dt}m\gamma v_y = -eE - e\alpha_y y, \tag{5.2b}$$

$$\frac{d}{dt}m\gamma v_z = -e\alpha_z z - ev_x B. \tag{5.2c}$$

For non-relativistic motion of the electrons, the relativistic γ factor is almost time independent, so we can write:

$$x'' + \omega_x^2 x = \beta z', \tag{5.3a}$$

$$y'' + \omega_y^2 y = -\omega_y^2 \eta, \tag{5.3b}$$

$$z'' + \omega_z^2 z = -\beta x', \tag{5.3c}$$

with $\omega_x^2 = \frac{e\alpha_x}{m\gamma}$, $\omega_y^2 = \frac{e\alpha_y}{m\gamma}$, $\omega_z^2 = \frac{e\alpha_z}{m\gamma}$, $\beta = \frac{eB}{m\gamma}$, $\omega_y^2\eta = \frac{eE}{m\gamma}$. The equations 5.3 mean that the motion in the y plane is decoupled from $x - z$ plane. The value of E is such that an electron in any position inside the bunch is extracted downwards, overcoming the attractive space charge potential of the beam.

The electron motion in the $x - z$ plane is given by the two coupled equations:

$$x'' + \omega_x^2 x = \beta z', \tag{5.4a}$$

$$z'' + \omega_z^2 z = -\beta x'. \tag{5.4b}$$

The total energy is therefore preserved in this plane

$$\frac{1}{2}v^2 + \frac{1}{2}\left[\omega_x^2 x^2 + \omega_z^2 z^2\right] = \frac{1}{2}v_0^2 + \frac{1}{2}\left[\omega_x^2 x_0^2 + \omega_z^2 z_0^2\right] \tag{5.5}$$

where $v_0 = \sqrt{\dot{x}_0^2 + \dot{z}_0^2}, x_0, z_0$ are the initial electron velocity and coordinates.

5.2 Low space charge limit

In absence of space charge the electron gyroradius is

$$\rho = \frac{v}{\beta}, \tag{5.6}$$

$\beta = \frac{eB}{m\gamma}$. Now we consider the case of very weak space charge. In this case, there is no relevant effect from the space charge on the electrons motion. However, the electron velocity will be tinily affected by the very weak space charge potential, but without changing significantly the gyroradius. The electron velocity and gyroradius will remain the initial one v_0 and $\rho_0 = \frac{v_0}{\beta}$.

The tiny variation of the velocity can be computed with the conservation law, equation 5.5. In fact, the variation of v for varying x, y is

$$v_0\Delta v + \omega_x^2 x_0 \Delta x + \omega_z^2 z_0 \Delta z = 0 \tag{5.7}$$

and for the very weak space charge case the maximum variation is again $|\Delta x|, |\Delta z| \leq 2\rho_0$ plus correction terms which we can neglect because the gyroradius practically does not change. Additionally $|\Delta x|, |\Delta z| < 2r_0$ with $r_0 = \sqrt{x_0^2 + z_0^2}$. Therefore

$$v_0 |\Delta x| < \left[\omega_x^2 x_0 + \omega_z^2 z_0\right] 2\rho_0 < \left[\omega_x^2 + \omega_z^2\right] 2r_0\rho_0. \tag{5.8}$$

The relative change of velocity becomes

$$\frac{|\Delta v|}{v_0} < \left[\omega_x^2 + \omega_z^2\right] 2r_0\rho_0 \frac{1}{v_0^2}. \tag{5.9}$$

Substituting v_0 with the initial gyroradius ρ_0 we obtain

$$\frac{|\Delta v|}{v_0} < \left[\omega_x^2 + \omega_z^2\right] 2r_0 \frac{1}{\beta^2\rho_0}. \tag{5.10}$$

The maximum variation of the electron velocity is expected for an electron generated at the edge of the beam of transverse radius R_b as

$$\frac{|\Delta v|}{v_0} < \left[\omega_x^2 + \omega_z^2\right] 2R_b \frac{1}{\beta^2\rho_0}. \tag{5.11}$$

In terms of the gyroradius we can also write

$$\frac{|\Delta \rho|}{\rho_0} < \left[\omega_x^2 + \omega_z^2\right] 2R_b \frac{1}{\beta^2\rho_0}. \tag{5.12}$$

Now we cal $D = \Delta\rho/\rho$ the relative difference we want to accept between the gyroradius with space charge ρ, and the initial gyroradius ρ_0 obtained without the space charge. Therefore the condition that the space charge will not alter the gyroradius more than D is

$$\frac{|\Delta \rho|}{\rho_0} < \left[\omega_x^2 + \omega_z^2\right] 2R_b \frac{1}{\beta^2\rho_0} < D. \tag{5.13}$$

Substituting the definitions we find

$$B^2 > \frac{\alpha_x + \alpha_z}{e} m\gamma \frac{2R_b}{D\rho_0} \tag{5.14}$$

which gives the condition on B so that the relative change in the gyroradius is less than D.

Now we consider the transverse space charge in the center of a Gaussian bunch. At $z = 0$, and for small x, y the transverse electric field is

$$E_x = \frac{1}{2\left(2\pi\right)^{3/2}\epsilon_0} \frac{eN}{\sigma_z\sigma_r^2} x, \tag{5.15}$$

where N is the number of protons in the bunch, σ_z the rms bunch length and σ_r the rms transverse radius. Hence

$$\alpha_x = \frac{1}{2\left(2\pi\right)^{3/2}\epsilon_0} \frac{N}{\sigma_z\sigma_r^2}. \tag{5.16}$$

We here assume that our uniform bunch has the maximum charge density of a Gaussian bunch hence α_x given by equation 5.16. Now we assume that $\alpha_x + \alpha_z \simeq \alpha_x$, which is a good approximation because for a long bunch $\alpha_x/\alpha_z \propto (\sigma_z/\sigma_r)^2$. Therefore if the field used in the BGI satisfies $B > B_t$, where

$$B_t = \sqrt{\frac{1}{2\left(2\pi\right)^{3/2}\epsilon_0} m\gamma \frac{1}{D}\frac{R_b}{\rho_0}\frac{N}{\sigma_z\sigma_r^2}}, \tag{5.17}$$

then the gyroradius of the electrons will have a relative error with respect to the gyroradius in absence of space charge less then D.

5.3 Space charge dominated regime

It was previously assumed that the electrons gyroradius is not altered too much by a space charge, which is the case for a week space charge case. However, if we increase the space charge and keep $B > B_t$ then the gyroradius ρ (with space charge) should not differ very much (less than D) from the gyroradius ρ_0 without space charge.

In the oder words: if in a strong space charge case we find that a stronger magnetic field B keeps the relative difference between ρ and ρ_0 less than D, then $B > B_t$ with B_t given by equation 5.17. The logic of this reasoning does not prevent the case in which $B > B_t$ and the relative error of the gyroradiuses is larger than D. It is, however, expected that by increasing B the gyroradius is "decreased" while the space charge will try to increase it. Therefore by increasing B there is a contrast to the action of space charge that would increase the particle velocity, hence increase the instantaneous gyroradius.

5.4 Strong field threshold verification

The equation 5.17 gives the threshold magnetic field necessary to keep the gyroradius increase smaller than D. One has to be aware that this formula was obtained after several assumption and requires the verification. The PyECLOUD simulation were used to verify whether the proportionality

$$B_t \propto \sqrt{\frac{N}{\sigma_z\sigma_r^2}} \tag{5.18}$$

is correct.

The simulation procedure was based on calculating the mean of the electrons velocity increase $\frac{\langle\Delta v\rangle}{\langle v_0\rangle}$ for a bunch of given parameters. The B_t value was tuned such that the velocity increase was of 10 %, $\frac{\langle\Delta v\rangle}{\langle v_0\rangle} = 0.1 = D$.

According to equation 4.3 ($\sigma_r = \sqrt{\varepsilon\beta/\gamma}$) σ_r depends on beam emittance ε, optical β function (which was kept constant in the simulations) and the beam energy E. The verification of

the proportionality 5.18 was performed by variation of the parameters:

- beam intensity N $(5 \cdot 10^{10} - 3 \cdot 10^{11})$,
- beam energy E $(450\ \mathrm{GeV} - 7\ \mathrm{TeV})$,
- beam emittance ε $(1\ \mu\mathrm{m} - 4.5\ \mu\mathrm{m})$,
- bunch length σ_z $(0.05\ \mathrm{cm} - 0.12\ \mathrm{cm})$

separately and plotting the obtained B_t dependence. The obtained plots are presented on figures 5.1 – 5.4.

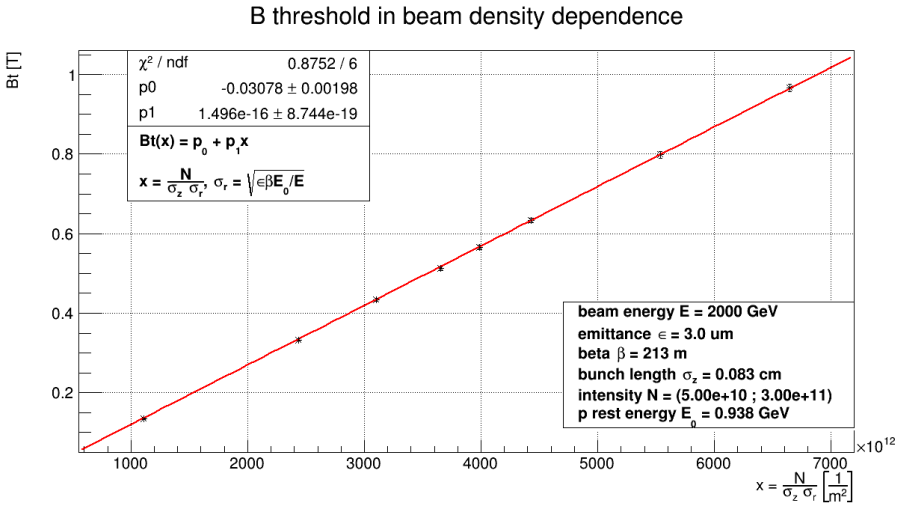

Figure 5.1: Magnetic field threshold B_t for beam intensity N variation.

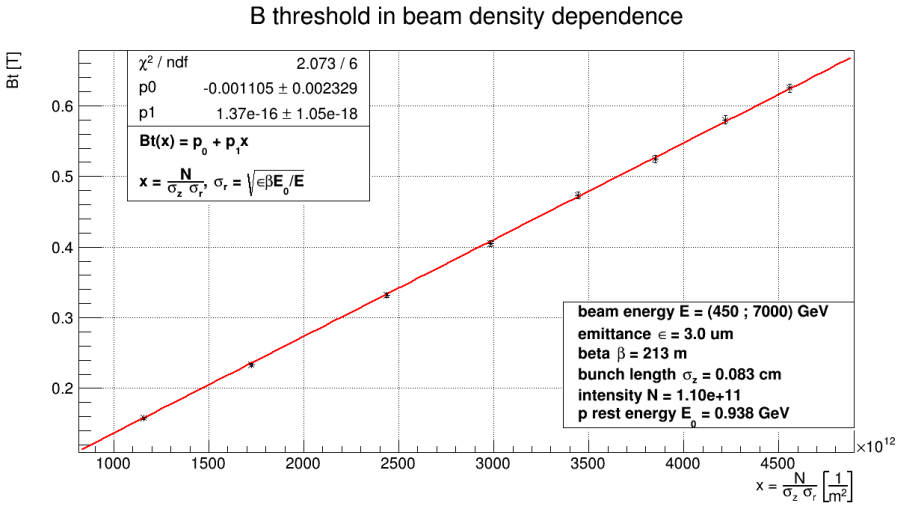

Figure 5.2: Magnetic field threshold B_t for beam energy E variation.

The label on the x axis is not an accident but a result of the simulation study. It turned out that the dependence of B_t on beam parameters is different than expected from theoretical

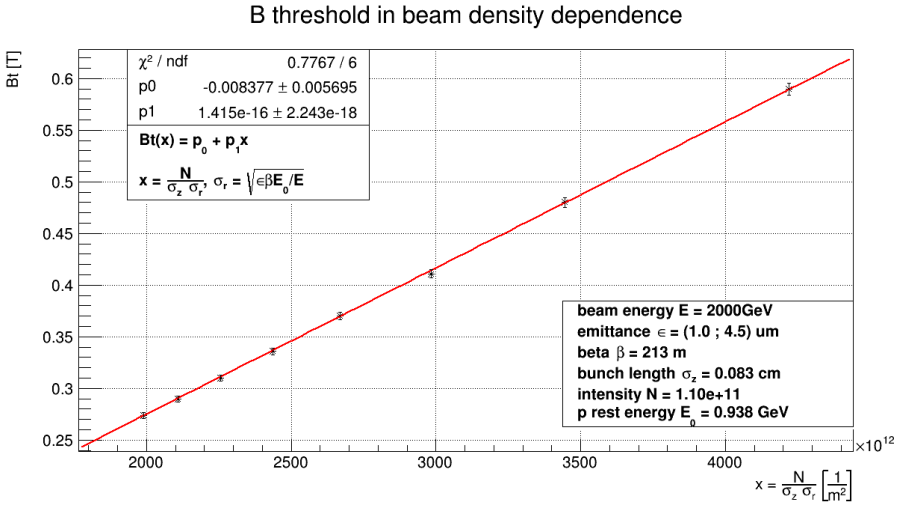

Figure 5.3: Magnetic field threshold B_t for emittance ε variation.

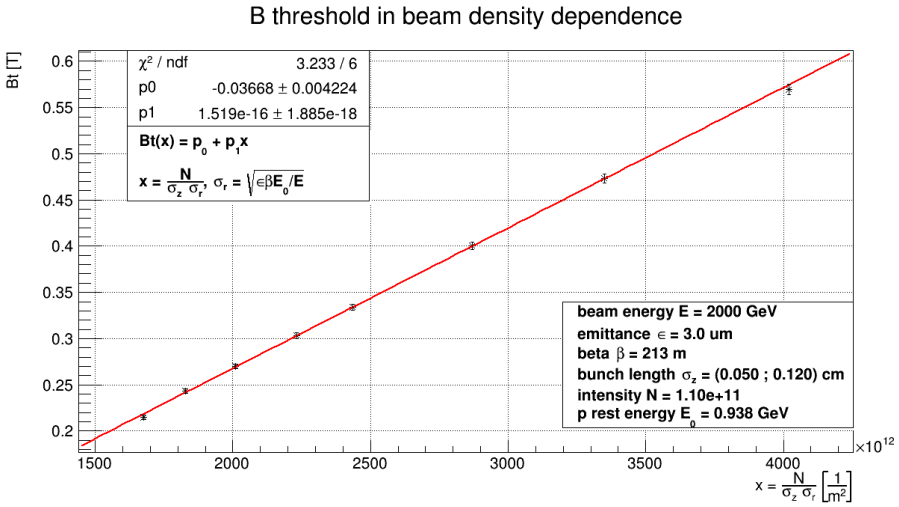

Figure 5.4: Magnetic field threshold B_t for bunch length σ_z variation.

model. It was found that B_t depends linearly on the $\frac{N}{\sigma_z \sigma_r}$ variable with a slope parameter of around $1.5 \cdot 10^{-16}$. This dependence can be approximated by

$$B_t = 1.5 \cdot 10^{-16} \frac{N}{\sigma_z \sigma_r} \tag{5.19}$$

The obtained formula allows to predict the magnetic field of the ionization chamber needed to dump the beam space charge impact and can be used for design an instrument similar to BGI.

Chapter 6

Conclusions

This thesis is a result of the research done during my internship at the European Organization for Nuclear Research, CERN. The main goal of this work was to analyze the Beam Gas Ionization monitor data and simulate the electron transport in the detector in order to study the effects of the electrons interaction with a high energy, dense particle beam.

As the Beam Gas Ionization monitor was design to measure the emittance of the ion beams and LHC mainly performs the proton beams, most of the data taken during the proton runs are not reliable and difficult to interpret. The reason for that is mainly the space charge which is strong for high intensity, small beam occurring for proton beams in LHC.

The BGI measurements of the ion beam show good agreement with the Wire Scanner and prove that BGI can be successfully used in case of ion beams. The few problems which occurred are probably caused by BGI hardware issues, which are understood and can be corrected, and by the size of an ion beam which was few times smaller (transverse emittance of $0.5\ \mu\mathrm{m}$ instead of $3.5\ \mu\mathrm{m}$) than initially predicted for LHC. For emittance of $0.5\ \mu\mathrm{m}$ the profile width depending on energy can reach from $800\ \mu\mathrm{m}$ to $200\ \mu\mathrm{m}$ which is close to BGI resolution, limited by pixel size calibration ($110\ \mu\mathrm{m}$) and electron gyroradius ($120\ \mu\mathrm{m}$).

The simulations of the electron transport in the BGI ionization chamber were mainly focused on investigation the space charge effects. It was shown that the proton beam is a source of a strong space charge which causes the electron velocity increase and influences the electron trajectories. As the result the profile broadening and distortion occurs.

It was also proposed to use the stronger magnetic field in order to dump the space charge effects. The simulations have shown that a magnetic field of $1\ \mathrm{T}$ is enough to reproduce the beam profile correctly and obtain right value of the beam emittance for proton beams with $\varepsilon \geq 1.5\ \mu\mathrm{m}$ and $\mathrm{N}_{\mathrm{proton}} \leq 1.6 \cdot 10^{11}$. The further investigation of this issue resulted in obtaining the empirical formula for magnetic field threshold needed to keep the space charge effects at the expected level.

The main benefit of this research is the understanding that a much higher magnetic field is

needed to ensure reliable measurements of the proton beam in the BGI. Some action was already performed in order to deliver the stronger magnets for BGI but this is a very cost consuming and logistically difficult process and will not be done before Run2 which starts in the beginning of 2015.

Bibliography

[1] CERN official website. http://www.cern.ch/

[2] ALICE Collaboration, K. Aamodt et al., *The ALICE experiment at the CERN LHC*,JINST 3 (2008) S08002.

[3] ATLAS Collaboration, *ATLAS Experiment at the CERN Large Hadron Collider*,JINST 3:S08003 (2008) 1–437.

[4] CMS Collaboration, R. Adolphi et al., *The CMS experiment at the CERN LHC*,JINST 3 (2008) S08004.

[5] LHCb Collaboration, A. Alves et al., *The LHCb Detector at the LHC*,JINST 3 (2008) S08005.

[6] M. Sapinski et al., *The first experience with the Beam Gas Ionization Monitor*, IBIC 2012.

[7] Microchannel Plates Principles of Operation http://ihea-www.cfa.harvard.edu/HRC/mcp/mcp.html

[8] Camera datasheet https://static.thermoscientific.com/images/D10423~.pdf

[9] T. Chapman, *Charge-Injection Devices Overcome Radiation Effects*, http://www.photonics.com/Article.aspx?AID=52489

[10] BGI website http://bgi.web.cern.ch/

[11] J. Rossbach and P. Schmuser., *Basic Course on Accelerator Optics*, volume 1. CERN report 94-01, 1994. CERN Accelerator School: Fifth General Accelerator Physics Course, University of Jyvaskyla, Finland, 7-18 September 1992.

[12] B. Salvant, *Impedance Model of the CERN SPS and Aspects of LHC Single-Bunch Stability*

[13] S.Y. Lee., *Accelerator Physics*. World Scientific, 2 edition, 2004.

[14] L. Ponce et al., *LHC Proton Beam Diagnostics Using synchrotron radiation.*, 2004 CERN Accelerators and beams department.

[15] F.Roncarolo et al., *Synchotron Radiation Measurements at the CERN LHC.* Prod. DIPAC 2011, Germany.

[16] J. Blasco, *Design of an optical fibre based angular position sensor for wire scanners complying with ultra-high vacuum, high temperature and radiation conditions of the CERN´s accelerators*, CERN 2012.

[17] G. Iadarola, G. Rumolo *PyECLOUD and build-up simulations at CERN*, CERN, Geneva, Switzerland.

[18] Geant4 simulation toolkit website `http://geant4.cern.ch/`

[19] D. H. Madison, *Angular Distributions of Electrons Ejected from Helium by Proton Impact*, PhysRevA.8.2449-1.

[20] M. Sapinski, *Geant4 simulation of electron trajectories in BGI*, CERN EDMS 1182412.

[21] A data analysis framework `http://root.cern.ch/`